G.W.C. Whiting
School of Engineering

The Johns Hopkins University

Effect of Microstructure on Passive Film Formation and Breakdown on Al Alloys

(grant # N00014-89-J-1180)

ANNUAL REPORT

by:

J. Kruger, J.W. Wagner, R.S. Lillard and C.C. Streinz
Materials Science and Engineering
Johns Hopkins University
Baltimore, Maryland 21218

P.J. Moran
Mechanical Engineering
United States Naval Academy
Annapolis, Maryland 21402

submitted to:
Dr. A. John Sedriks
Materials Division (Code 1131)
Office of Naval Research
Arlington, Virginia 22217

Effect of Microstructure on Passive Film Formation and Breakdown on Al Alloys

(grant # N00014-89-J-1180)

ANNUAL REPORT

by:

J. Kruger, J.W. Wagner, R.S. Lillard and C.C. Streinz
Materials Science and Engineering
Johns Hopkins University
Baltimore, Maryland 21218

P.J. Moran
Mechanical Engineering
United States Naval Academy
Annapolis, Maryland 21402

submitted to:
Dr. A. John Sedriks
Materials Division (Code 1131)
Office of Naval Research
Arlington, Virginia 22217

4. PERFORMING ORGANIZATION REPORT NUMBER(S)		5. MONITORING ORGANIZATION REPORT NUMBER(S)	
N00014-89-J-1180		paspool---03	
6a. NAME OF PERFORMING ORGANIZATION Johns Hopkins University	6b. OFFICE SYMBOL *(If applicable)*	7a. NAME OF MONITORING ORGANIZATION Materials Division Code 1131M Office of Naval Research	
6c. ADDRESS *(City, State, and ZIP Code)* 102 Maryland Hall Baltimore, MD 21218		7b. ADDRESS *(City, State, and ZIP Code)* 800 North Quincy Street Arlington, VA 22217-5000 Attn: A. John Sedriks	
8a. NAME OF FUNDING/SPONSORING ORGANIZATION ONR	8b. OFFICE SYMBOL *(If applicable)*	9. PROCUREMENT INSTRUMENT IDENTIFICATION NUMBER	
8c. ADDRESS *(City, State, and ZIP Code)* 800 North Quincy Street Arlington, VA 22217-5000		10. SOURCE OF FUNDING NUMBERS	
		PROGRAM ELEMENT NO.	PROJECT NO. / TASK NO. / WORK UNIT ACCESSION NO.

11. TITLE *(Include Security Classification)*

Effect of Microstructure on PassiveFilm Formation and Breakdown on Al Alloys

12. PERSONAL AUTHOR(S)

J. Kruger, J.W. Wagner, R.S. Lillard, C.C. Streinz, and P.J. Moran

13a. TYPE OF REPORT	13b. TIME COVERED	14. DATE OF REPORT *(Year, Month, Day)*	15. PAGE COUNT
Annual	FROM 12/15/90 TO 12/14/91	92-1-27	69

16. SUPPLEMENTARY NOTATION

17. COSATI CODES			18. SUBJECT TERMS *(Continue on reverse if necessary and identify by block number)*
FIELD	GROUP	SUB-GROUP	Al alloys, passive films, breakdown, microstructure, dynamic imaging microellipsometry, local electrochemical impedance spectroscopy

19. ABSTRACT *(Continue on reverse if necessary and identify by block number)*

Dynamic imaging microellipsometry (DIM) has been utilized to examine the passive film growth on a dynamically compacted Al-1%Ta alloy produced by Martin Marietta Laboratories. SEM observation revealed Al_3Ta precipitates up to 20 microns in diameter. These precipitates were identified ellipsometrically demonstrating *in-situ* spatial resolution of at least 20 microns. In addition it was observed that a thinner passive film formed over the precipitates than over the matrix material. This may result in an incompatibility between the two films that results in local strains or flaws, such as dislocations, that promote Cl^- ingress and degrade the protective nature of the passive film.

Ellipsometric analysis of the passivation of Al-8at%Ta and Al-11at%W has demonstrated that the passive films formed on the alloys are thinner than on pure aluminum. To a first approximation

20. DISTRIBUTION/AVAILABILITY OF ABSTRACT	21. ABSTRACT SECURITY CLASSIFICATION	
☐ UNCLASSIFIED/UNLIMITED ☐ SAME AS RPT. ☐ DTIC USERS	Unclassified	
22a. NAME OF RESPONSIBLE INDIVIDUAL Jerome Kruger	22b. TELEPHONE *(Include Area Code)* 410-516-8937	22c. OFFICE SYMBOL

19. Abstract - continued

the film thickness on both alloys is half that of pure aluminum at a given applied potential. It has also been observed that the index of the passive film on the Al-W alloy increases at an applied overpotential of approximately 1 volt.

The scanning electrochemical impedance spectroscopy (EIS) technique developed during the first two years has been improved and quantitatively demonstrated. This was accomplished by examining two electrochemical systems. The first was a homogeneous 99.999% aluminum electrode. The area normalized scanning impedance data generated for the homogeneous electrode agreed with the area normalized data generated with traditional EIS methods within 10%. The agreement is expected if the electrode is perfectly homogeneous.

To demonstrate that this technique could be used to accurately locate and measure the impedance properties of surface heterogeneities, a second system containing a model defect was examined. The model defect was constructed by force molding 99.999% aluminum around a 100 um diameter molybdenum wire. Not only was the scanning impedance system able to accurately locate the Mo wire in this electrode, but it also generated area normalized impedance data for the aluminum and molybdenum portions of the electrode that agreed with area normalized traditional impedance measurements on bulk Al and Mo under the same electrochemical conditions within 15%.

A. Description of Scientific Research Goals

The goal of this program is to understand how the composition and microstructure of aluminum and its alloys influence the factors that control the phenomenon of passivity breakdown that results in the initiation of pitting corrosion. In order to accomplish this goal two new *in-situ* high spatial resolution experimental methods were proposed and have been developed and demonstrated. These are dynamic imaging microellipsometry and scanning electrochemical impedance spectroscopy. In addition a scanning tunneling microscope has been recently acquired and will enable examination of corrosion processes on an atomistic size scale

B. Techniques for In-Situ Study of Localized Corrosion Processes

B1. Dynamic Imaging Microellipsometry:

Ellipsometry is an optical technique that enables the thickness and complex refractive index of thin films on metal surfaces to be measured *in-situ* [1]. Since many corrosion and electrochemical processes involve film formation and breakdown, ellipsometry has proven to be a valuable research tool for studying corrosion [2]. Traditional ellipsometry, however is by nature a surface averaging technique and is limited for studying localized corrosion processes such as the effects of microstructure on passive film growth and breakdown.

Several investigators [3-6] have attempted to overcome this limitation by scanning single point ellipsometric measurements over a surface of interest. Sugimoto et al. [4,5], examined passive films on duplex stainless steels and reported a spatial resolution of approximately 10 microns. While a scanning approach can be used to observe localized features, it has poor

temporal resolution. One commercial instrument [7] specifies 4 seconds per point, corresponding to 11 hours for acquisition of a 100x100 pixel image. Hurd and Brinker [8,9] have devised an imaging system that tracks several discrete nulls for drying sol gel films. Useful spatial information is obtained from this method, however, it does not yield a quantitative full field ellipsometric analyses of the illuminated area since not all regions of the drying film satisfy the null conditions.

Recently, Cohn et al. [10-15] developed dynamic imaging microellipsometry (DIM). In contrast to the Hurd and Brinker [8,9] technique, DIM is a *radiometric* full field imaging approach to ellipsometry. Good spatial resolution (approximately 20 microns) and precision in addition to good temporal resolution (minutes) was demonstrated. The DIM approach utilized the standard polarizer, specimen, compensator, analyzer (PSCA) ellipsometry configuration in combination with an imaging lens, a CCD video camera and digital image processing techniques to acquire high spatial resolution ellipsometric data with good temporal resolution. An analytical description of the system was derived utilizing the Jones matrix and vector formalisms [11,12]. The intensity at the CCD detector for a given initial polarization angle was described as a function of three variables, the ellipsometric parameters Δ and ψ, and the system gain. Since the intensity equation contained three unknowns (Δ, ψ and gain) it was not directly solvable. The approach taken involved digitizing a minimum of three intensity images, each at a unique initial polarization angle. The independent equations obtained were then used to solve directly for Δ and ψ. Δ and ψ maps were calculated point by point from the digitized intensity images recorded at their respective polarization states. These Δ and ψ maps were referred to as ellipsograms.

B2. Local Electrochemical Impedance Spectroscopy:

AC impedance (also known as Electrochemical Impedance Spectroscopy, EIS) is a powerful non-destructive in situ technique which has been used extensively to investigate electrochemical systems [16-19]. In the conventional EIS approach, a small sinusoidal voltage perturbation is applied across the electrochemical interface. Because, however, the current response of the whole electrode is used to generate impedance data a surface averaged measurement results which can lead to difficulties when interpretating data if the behavior is not uniform over the entire electrode interface; as is the case in localized corrosion systems [20]. Although EIS has been applied to localized corrosion systems, data analysis for these systems is complex [21-24]. For this reason, to investigate localized corrosion due to multi-phases, grain boundary effects, or other surface heterogeneities which may occur on an electrode surface a method of generating local ac impedance data is preferable.

Recently Isaacs and Kendig [25], as well as other investigators [26-27] have combined scanning technology with impedance methods in an attempt to generate local ac impedance data for discrete areas on electrodes. In these techniques, the electrode to be examined was polarized locally with a small disc shaped probe that contained "micro" reference and counter electrodes. In an attempt to confine the current generated by the local polarization to the area of interest, a thin layer cell geometry was employed. While this technique has been used to generate qualitative results, no quantitative local ac impedance data has been produced with this method.

In the first two years of this program a novel method for generating **quantitative** local ac impedance data has been developed. The technique is founded on the basic premiss that the local ac solution current densities *very* near the working electrode, in a conventional three

electrode ac impedance measurement, are proportional to the local impedance properties of the electrode. Further, the local ac current responses to the applied sinusoidal voltage perturbation signal may be measured with a two electrode micro-probe, developed in this program. By measuring the ratio of the applied voltage perturbation to the local ac solution current density, measured with this probe, a local electrochemical impedance measurement results. The accuracy and resolution of this technique have been demonstrated [28-29] and are capsulized later in this proposal.

C. Significant Results in Past Year

A third generation dynamic imaging microellipsometry (DIM) system has been developed and assembled. It features enhanced temporal resolution and data acquisition capabilities. Ellipsogram to ellipsogram temporal resolution for the present system is 20 seconds and is limited by the rotation speed of the half wave plate. DIM has been utilized to examine the passive film growth on a dynamically compacted Al-1%Ta alloy produced by Martin Marietta Laboratories. SEM observation revealed Al_3Ta precipitates up to 20 microns in diameter. These precipitates were identified ellipsometrically demonstrating *in-situ* spatial resolution of at least 20 microns. In addition it was observed that a thinner passive film formed over the precipitates than over the matrix material. This may result in an incompatibility between the two films that results in local strains or flaws, such as dislocations, that promote Cl^- ingress and degrade the protective nature of the passive film. This work was reported at the Spring 1991 ECS meeting in Washington, D.C. It has also been submitted to the Journal of the Electrochemical Society for publication [30].

Ellipsometric analysis of the passivation of Al-8at%Ta and Al-11at%W is underway. Consistent with the observations of Shaw et al. [31] and Davis et al. [32], this analysis dem-

onstrates that the passive films formed on the alloys are thinner than on pure aluminum. To a first approximation the film thickness on both alloys is half that of pure aluminum at a given applied potential. It has also been observed that the index of the passive film on the Al-W alloy increases at an applied overpotential of approximately 1 volt. This is consistent with Shaw et al. [31] who observed sharply increasing concentrations of WO_2 and WO_3 in the passive film at an applied overpotential of 1 volt. Passivity and breakdown of these systems is the subject of continued investigation.

During the first two years of this program a scanning electrochemical impedance spectroscopy (EIS) technique has also been developed and quantitatively demonstrated [28-29]. This was accomplished by examining two electrochemical systems. The first was a homogeneous 99.999% aluminum electrode. The area normalized scanning impedance data generated for the homogeneous electrode agreed with the area normalized data generated with traditional EIS methods within 10%. The agreement is expected if the electrode is perfectly homogeneous.

To demonstrate that this technique could be used to accurately locate and measure the impedance properties of surface heterogeneities a second system containing a model defect was examined. The model defect was constructed by force molding 99.999% aluminum around a 100 um diameter molybdenum wire. Not only was the scanning impedance system able to accurately locate the Mo wire in this electrode but it also generated area normalized impedance data for the aluminum and molybdenum portions of the electrode that agreed with area normalized traditional impedance measurements on bulk Al and Mo under the same electrochemical conditions within 15%. This work was reported at the Spring 1991 ECS meeting in Washington, D.C. It has also been submitted to the Journal of the Electrochemical Society for publication [29].

Appendix 1: C.C. Streinz, J.W. Wagner, J. Kruger, P.J. Moran, "Analysis of Passive Film Growth by Dynamic Imaging Microellipsometry," J. Electrochem. Soc., In Press.

Appendix 2: R.S. Lillard, P.J. Moran, H.S. Isaacs, "A Novel Method for Generating Local Electrochemical Impedance Spectroscopy," J. Electrochem. Soc., In Press.

D. References

[1] R.M.A. Azzam and N.M. Bashara, Ellipsometry and Polarized Light, Elsevier Science Publishers, New York (1987).

[2] J. Kruger, J. Physique 38, Colloque C-5, supplement to No. 11, CS 129-CS 138 (1977).

[3] D.J. Dunlavy, R.B. Hammond and R.K. Ahrenkiel, Los Alamos National Labs Report LA-UR-81-1806, 6p (1981).

[4] K. Sugimoto and S. Matsuda, J. Electrochem. Soc., 130 (12), 2323 (1983).

[5] K. Sugimota, S. Matsuda, Y. Ogiwara and K. Kitamura, J. Electrochem. Soc., 132 (8), 1791 (1985).

[6] M. Erman and J.B. Theetan, Journal of Applied Physics, 60 (3), 859 (1986).

[7] "Auto Gain Ellipsometers," Bulletin EE, Gaertner Scientific Corporation, p. 13.

[8] A.J. Hurd and C.J. Brinker, J. Physique, 49 (6), 1017 (1988).

[9] A.J. Hurd and C.J. Brinker, in Better Ceramics through Chemistry III, Brinker, Clark and Ulrich, Eds., Materials Research Society, (1988).

[10] R.F. Cohn, J.W. Wagner, and J. Kruger, J. Electrochem. Soc., 135 (4), 1033 (1988).

[11] R.F. Cohn, J.W. Wagner, and J. Kruger, Appl. Opt., 27 (22), 4664 (1988).

[12] R.F. Cohn and J.W. Wagner, in "Review of Progress in Quantitative NDE", 8B, D.O. Thompson and D.E. Chimenti, Eds., 1219 (1989).

[13] R.F. Cohn and J.W. Wagner, in "Proceedings of of the Society for Photo-optical Instrument Engineering," 1036, 125 (1989).

[14] R.F. Cohn and J.W. Wagner, Appl. Opt., 28, 3187 (1989).

[15] R.F. Cohn, Appl. Opt., 29 (2), 304 (1990).

[16] Macdonald, J.R., ed., Impedance Spectroscopy, (New York: Wiley, 1987).

[17] Epelboin, I., Gabrielli, C., Keddam, M., and Takenouti, H., in: Electrochemical Corrosion Testing, ASTM STP 727, F. Mansfeld and U. Bertocci eds., ASTM, 1981, pp 150-166.

[18] Macdonald, D. D., and McKubre, M. C. H., Electrochemical Corrosion Testing, ASTM STP 727, F. Mansfeld and U. Bertocci eds., ASTM, 1981, pp. 110-149.

[19] Kelly, R.G., Moran, P.J., **The Journal of the Electrochemical Society**, vol. 134, no. 1, 1987.

[20] McKubre, M.C.H., paper # 480, NACE, Corrosion 87, San Francisco Ca., March 1987.

[21] Kendig, M. W., and Mansfeld, F., **Proc. Fall Meeting of the Electrochemical Soc.**, Vol. 82-2, pp 105-6, 1982.

[22] Oltra, R., Keddam, M., **Corrosion Science**, Vol. 28, No. 1, pp. 1-18. 1988.

[23] Juttner, K., Lorenz, W. J., Kendig, M. W., Mansfeld, F., Journal of the Electrochemical **Society**, Vol. 135, No. 2, pp. 332-39, 1988.

[24] Hitzig, J., Juttner, K., Lorenz, W. J., **Journal of the Electrochemical Society**, Vol. 133, No. 5, pp. 887-892, 1986.

[25] Isaacs, H. S., and Kendig, M. W., **Corrosion**, Vol. 36, pp. 269-74, 1980.

[26] Hughes, M. C., and Parks, J. M., in Corrosion Control by Organic Coatings, H. Leidheiser Jr. ed., NACE, Houston TX, 1981.

[27] Standish, J.V., Leidheiser Jr., H., **Corrosion**, vol 36, no. 8, NACE, 1980.

[28] R.S. Lillard, Master's Essay, Johns Hopkins University, 1990.

[29] R.S. Lillard, P.J. Moran, and H.S. Isaacs, submitted to J. Electrochemical Society, June 1991.

[30] C.C. Streinz, J.W. Wagner, J. Kruger and P.J. Moran, submitted to J. Electrochemical Society, June 1991.

[31] G.D. Davis, W.C. Moshier, T.L. Fritz, and G.O. Cote, J. Electrochem. Soc., 137, 422 (1990)

[32] B.A. Shaw, G.D. Davis, T.L. Fritz, B.J. Rees, and W.C. Moshier, J. Electrochem. Soc., 138(11), 3288 (1991).

APPENDIX 1

Analysis of Passive Film Growth by Dynamic Imaging Microellipsometry

(revised October 31, 1991)

C.C. Streinz[1], J.W. Wagner, J. Kruger[2]
Department of Materials Science and Engineering
The Johns Hopkins University
Baltimore, Maryland 21218

P.J. Moran[2]
Department of Mechanical Engineering
United States Naval Academy
Annapolis, Maryland 21402

Abstract:

Dynamic Imaging Microellipsometry (DIM) is a full field, radiometric approach to ellipsometry that provides high spatial resolution and accuracy. This paper reports on the latest DIM system and demonstrates the usefulness of the DIM technique for *in-situ* examination of passive film growth on materials with microstructural inhomogeneities. In particular DIM has been utilized to examine passive film growth on a polycrystalline iron sample and an aluminum tantalum alloy that contained intermetallic precipitates. Grain orientation has been observed to affect the growth rate and final thickness of the film on iron. Ellipsometric identification of intermetallic precipitates (approximately 20 microns in diameter) is reported. The precipitates are observed to form a thinner passive film than the matrix. The incompatibility between the film over the precipitate and that over the matrix may degrade the localized corrosion behavior of these alloys.

---

1 Electrochemical Society Student Member

2 Electrochemical Society Active Member

Introduction:

Ellipsometry is an optical technique that enables the thickness and complex refractive index of thin films on metal surfaces to be measured *in-situ* [1]. Since many corrosion and electrochemical processes involve film formation and breakdown, ellipsometry has proven to be a valuable research tool for studying corrosion [2]. Traditional ellipsometry, however is by nature a surface averaging technique and is limited for studying localized corrosion processes such as the effects of microstructure on passive film growth and breakdown.

Several investigators [3-6] have attempted to overcome this limitation by scanning single point ellipsometric measurements over a surface of interest. Sugimoto et al. [4,5], examined passive films on duplex stainless steels and reported a spatial resolution of approximately 10 microns. While a scanning approach can be used to observe localized features, it has poor temporal resolution. One commercial instrument [7] specifies 4 seconds per point, corresponding to 11 hours for acquisition of a 100x100 pixel image. Hurd and Brinker [8,9] have devised an imaging system that tracks several discrete nulls for drying sol gel films. Useful spatial information is obtained from this method, however, it does not yield a quantitative full field ellipsometric analyses of the illuminated area since not all regions of the drying film satisfy the null conditions.

Recently, Cohn et al. [10-15] developed dynamic imaging microellipsometry (DIM). In contrast to the Hurd and Brinker [8,9] technique, DIM is a *radiometric* full field imaging approach to ellipsometry. Good spatial resolution (approximately 20 microns) and precision in addition to good temporal resolution (minutes) was demonstrated. The DIM approach utilized the standard polarizer, specimen, compensator, analyzer (PSCA) ellipsometry con-

figuration in combination with an imaging lens, a charge coupled device (CCD) video camera and digital image processing techniques to acquire high spatial resolution ellipsometric data with good temporal resolution.

The purpose of this paper is to report on the latest DIM system and to demonstrate the usefulness of this technique for examining passive film growth on materials with microstructural inhomogeneities. Results are reported for passive film growth on a polycrystalline iron sample and an aluminum tantalum alloy that contained intermetallic precipitates.

Dynamic Imaging Microellipsometry Theory and System Design

A block diagram of the DIM system used in this study is illustrated in Figure 1. The conventional PSCA optics are used in combination with a 105 mm Nikkor imaging lens and a Pulnix TM-34K CCD video camera in the focal plane. A half-wave plate mounted in an Oriel computer controllable rotation stage is inserted after the polarizer and is used to rotate the plane of the linearly polarized light while the polarizer remains fixed [12]. A Hewlett Packard HLMP-8150 ultrabright light emitting diode was used as the light source and provided quasimonochromatic light of wavelength 650 nm. The ultrabright diode was used instead of a laser source to eliminate the speckle interference associated with highly monochromatic light [16].

An analytical description of the system was derived utilizing the Jones matrix and vector formalisms [11,12]. The intensity at the CCD detector for a given initial polarization angle is described as follows.

$$I(P) = \frac{G^2}{2}\{a\cos^2 P\tan^2\psi + b\sin^2 P + (c\cos\Delta - d\sin\Delta)\sin 2P\tan\psi\} \qquad (1)$$

where:

$$a = 1 + \cos 2C \cos 2(A - C)$$

$$b = 1 - \cos 2C \cos 2(A - C)$$

$$c = \sin 2C \cos 2(A - C)$$

$$d = \sin 2(A - C)$$

G is the system gain (related to the optical components), and A and C are the analyzer and compensator azimuth angles respectively, and Δ and ψ are the ellipsometric parameters of interest. The parameter Δ is the change in phase and $\tan\psi$ the change in relative amplitude between the orthogonal components of the electric field vector of the incident light. Since Equation 1 contains three unknowns (Δ, ψ and G) it is not directly solvable. The approach taken involves digitizing a minimum of three intensity images, each at a unique initial polarization angle. The independent equations obtained are then used to solve directly for Δ and ψ. A four image algorithm where images are captured at initial polarization states of -45°, 0°, 45°, and 90° is shown below and was used for computational ease in this study.

$$\Delta = \cos^{-1}\left(\frac{I(45°) - I(-45°)}{2\sqrt{I(0°)I(90°)}}\right) - \tan^{-1}\left(\frac{d}{c}\right) \qquad (2)$$

$$\psi = \tan^{-1}\left(\sqrt{\frac{I(0°)}{I(90°)}}\sqrt{\frac{b}{a}}\right) \qquad (3)$$

Δ and ψ maps are calculated point by point from the digitized intensity images recorded at the four initial polarization states (I(-45°), I(0°), I(45°), and I(90°)) using Equations 2 & 3. The Δ and ψ maps are hereafter referred to as ellipsograms. A sample ellipsogram of a silicon wafer is illustrated in Figure 2. Note that the gray levels observed are linearly proportional

to Δ and ψ. The wafer is covered with an SiO_2 film that has a gradient in thickness from approximately 30 to 50 nm owing to nonuniform growth conditions. The variation in film thickness from the upper left corner to the lower right corner is easily observed in the figure.

The system was automated by a Personal Computer with an 80386 microprocessor, an 80387 math coprocessor and a Data Translations DT2862 Arithmetic Frame Grabber that digitizes 480 video lines with 512 pixels in each line. Data acquisition and processing utilized the algorithm described in Equations 2 & 3. The software also enabled ellipsograms to be computed using two distinct three image algorithms reported by Cohn [15]. Acquisition time for three images is approximately 7.5 seconds, while for four images 10.75 seconds is required. Ellipsogram to ellipsogram temporal resolution for the three and four image algorithms are 20 and 21 seconds respectively. Temporal resolution for the present system is limited by the rotation speed of the half wave plate.

Experimental

Polycrystalline Iron Parameters: A 99.99% pure iron sample with grains that were up to 2 mm in diameter was examined via DIM. All measurements were made in a pH 7.2 sodium borate - boric acid buffer solution. The specimens were prepared by abrading through 4000 grit paper. The final surface polish was performed with a 0.25 micron diamond aerosol spray. Prior to anodic polarization the sample was polarized to -950 mV SCE to remove the air formed oxide. The specimen was then polarized to 500 mV SCE for nearly 5 hours. Formation of the passive film was monitored via DIM. Ellipsograms were acquired at 60 second intervals for the first 13 minutes, 10 minute intervals for the following 90 minutes and 30 minute intervals for the final 3 hours. The ellipsometric parameters, Δ and ψ, were monitored for various grains during passive film growth and plotted versus log time. An approximate orientation

of several of the grains of interest was determined by SEM examination following etching in a 10% Nital solution. The Nital solution preferentially attacks the iron exposing (100) planes [17].

Aluminum Tantalum Alloy Parameters: A section from an Al-1at%Ta alloy prepared via dynamic compaction of atomized alloy powders was analyzed via DIM. SEM characterization of the alloy showed aluminum tantalum (probably Al_3Ta [18]) precipitates up to 20 microns in diameter as illustrated in Figure 3. As a result this alloy provided an excellent control sample for determination of spatial resolution of DIM in solution. All measurements were made in a pH 7.2 sodium borate - boric acid buffer solution. The specimen surfaces were prepared by dry abrading the specimen through 4000 grit paper. Abrasion was carried out under dry conditions to avoid galvanic interactions between the precipitates and the matrix material. The final surface polish was performed using a 0.25 micron diamond aerosol spray. SEM analysis showed no visible galvanic attack during the polishing. It should be noted, however, that, even after polishing, these alloys had a surface roughness or texture of the order of 10's of microns resulting from the dynamic compaction forming technique. This provided difficulties in the ellipsometric analysis and will be discussed later. The polarization behavior of this alloy was determined via potentiodynamic polarization scans. The alloy was scanned from open circuit (approximately -980 mV SCE) to 1200 mV SCE at a scan rate of 0.2 mV per second. Ellipsograms were acquired at 400 mV intervals during the scan.

Results and Discussion

Polycrystalline Iron: Figure 4 is an ellipsogram of the polycrystalline iron sample acquired after 5 hours of polarization at 0.5 volts SCE. Recall that Δ and ψ are linearly proportional to the gray levels in the their respective maps. Note that the grain structure of the sample is

"observable" in the Δ map but not in the ψ map, indicating differences in the passive film thickness over the respective grains. If the difference observed were only owing to surface roughness, the grain structure would also be "observable" in the ψ map since ψ is sensitive to roughness [19]. It should also be pointed out that orientation effects are minimized when the film is reduced providing further support that the grain structure "observed" in Figure 4 is the result of film thickness differences.

Figure 5 is a plot of the change in Δ versus log time for the grains labeled 1 and 2 in Figure 4 at 0.5 volts SCE. Negative "$\delta\Delta$" is linearly proportional to change in film thickness for small film thickness [20]. Therefore Figure 5 illustrates that the growth of the passive film is dependent on the orientation of the substrate. Grain 1 in Figure 4 is close to a (111) orientation while grain 2 is close to (100) as determined by examination of etched surfaces in an SEM. Neither grain was oriented precisely. Using McCrackin's program [21] it was determined that the final difference in film thickness between the two grains was approximately 0.4 nm. The final thickness for grain 2 was approximately 3.6 nm compared to approximately 3.2 nm for grain 1. Dependence of film growth rate on grain orientation on iron has been observed by Kruger and Calvert [22] by comparing measurements made on single crystals. Orientation effects were expected since the passive film on iron is known to be crystalline [23-25]. DIM enables the effects of microstructure on the growth of the passive film on iron to be directly observed on a polycrystalline sample. The DIM technique is well suited to studying surface phenomenon, such as passive film growth, that are dependent on grain orientation.

Similar measurements have been performed on a 99.999% pure polycrystalline aluminum sample. No dependence on orientation of passive film growth was observed. This is not surprising since the passive films on aluminum have been shown to be amorphous [26].

Aluminum Tantalum Alloys: Aluminum alloys containing solid solution additions of tantalum exhibit a markedly increased resistance to pitting corrosion [27-28]. The improvement however is degraded by the presence of intermetallic precipitates [29] such as those observed in the dynamically compacted alloy used in this study. Determination of the properties of the passive film over the precipitates would aid in understanding the breakdown processes of these alloys. The polarization behavior of the dynamic compacted Al-1.0at%Ta alloy in pH 7.2 borate buffer solution is illustrated in Figure 6. The increase in current at approximately 1100 mV SCE is owing to the onset of O_2 evolution. This result was surprising since on pure aluminum the O_2 evolution reaction is not observed. Neither is it observed on solid solution Al-8at%Ta in the same electrolyte [30]. In addition, Frankel et al. [28] observed pitting potentials of 1600 mV SCE for an Al-41at%Ta solid solution alloy in 0.1M NaCl and reported no O_2 evolution prior to breakdown. Another aluminum alloy with 10at% solid solution additions of tungsten rather than tantalum exhibited pitting potentials of nearly 2000 mV SCE in 0.1M NaCl and also reported no O_2 evolution prior to breakdown [31]. Since the O_2 evolution reaction is not observed on solid solution Al-Ta and Al-W alloys nor on pure aluminum or a solid solution Al-8at%Ta alloy in a pH 7.2 borate buffer solution containing no Cl^-, it is concluded that the reaction occurs at the precipitates in the alloy used in this study. Further evidence is supplied by SEM and XRM analysis of the dynamically compacted alloys that shows no evidence of impurities that might act as sites for O_2 evolution.

As stated in the Experimental Section surface preparation was difficult. Repeated attempts at producing an optically flat surface on these specimens failed. The textured surfaces resulted in textured ellipsograms and interfered with locating and ellipsometrically analyzing the intermetallic precipitates in these alloys. Figure 7 is an ellipsogram of the alloy at E_{corr} that demonstrates the effects of the surface texture on the ellipsometric data. Spatial variations

of several degrees in Δ and ψ are evident. It should be pointed out, however, that Figure 7 demonstrates that the DIM technique provides a method for examining surface roughening *in-situ*.

Despite the severity of the surface roughness, precipitates were observed and qualitatively analyzed ellipsometrically. To locate the precipitates the sample was first polarized to 2000 mV SCE and held at that potential until O_2 bubbles formed on the surface. As described above, it was concluded that the O_2 evolution reaction occurs at the precipitates. After digitally locating the bubbles the previously generated ellipsograms were analyzed in the regions where bubbles formed. Figure 8 illustrates what was observed ellipsometrically in these locations. The right side of the figure is a polarized light photograph of the region around one of the bubbles. The bubble appears as a doublet because it shades both the incident and reflected beam. The left side of the figure is a Δ map of the same region. Note the dark area in the center of the box, corresponding to a lower value of Δ for that region. This region is the Δ value over one of the precipitates in the alloy. The size of the region is approximately 20 microns. At the magnification used each pixel is approximately 4-5 microns square. At E_{corr} (-980 mV SCE) where the passive film is thin, the Δ measured for the precipitate is approximately 3 degrees less than that for the matrix. It was also observed that ψ was approximately 1.5 degrees higher for the precipitate than over the matrix. This probably results from different refractive index values for the substrate.

Figure 9 plots $(-\delta\Delta)$ versus applied potential for the precipitate and the matrix material. Note that the slope of $(-\delta\Delta)$ versus applied potential for the precipitate is less than that of the matrix, indicating that to a first approximation the precipitate forms a thinner film at a given applied potential than the matrix. Consideration of the film indicies lends further support to this conclusion. Muth [32] measured the index of Ta_2O_5 is 2.22. The index of Al_2O_3 is

1.65 [33]. He also measured a film index of 2.12 for an Al-73at%Ta alloy. Therefore it is expected that the index of the precipitate passive film to be between that of pure Ta_2O_5 and pure Al_2O_3, hence an index that is higher than that of Al_2O_3. This supports the contention that the precipitate passive film is thinner than the matrix passive film since forming a passive film with a greater index results in a greater decrease in Δ for a given film thickness. Therefore, even if the slopes were identical in Figure 9 it would indicate a thinner film on the precipitate. Assuming an index of 1.79 for the passive film on Al_3Ta (based on a law of mixtures approximation) and an index of 1.65 for the passive film on the matrix (the same for the passive film on aluminum), a final matrix passive film thickness of approximately 7.0 nm and a final precipitate passive film of approximately 4.5 nm were calculated. This may result in an incompatibility between the two films causing local strains or flaws such as dislocations that promote Cl^- ingress and degrade the protective nature of the passive film. The role of defects in the breakdown of aluminum is controversial and has been discussed considerably (see review by Foley [34]). Quantitative comparison of the films over the precipitate and matrix is difficult owing to the surface roughness of the alloy. The purpose here is instead to demonstrate that features of the order of 20 microns are observable ellipsometrically (even on a specimen that is far from ideal) and that determination of passive film parameters on these features is possible in solution. In future experiments, sputtered alloys that are optically flat and smooth (similar to those described previously [27,31,35]) will be examined. This will decrease spatial noise significantly and enable better evaluation of the passive films and their dependence on microstructure.

Conclusions:

This paper reports on the latest DIM system and demonstrates the usefulness of the DIM technique for *in-situ* examination of passive film growth on materials with microstructural inhomogeneities. On polycrystalline iron it was shown that the thickness and growth kinetics of the passive film were dependent on the grain orientation. Grain to grain thickness variations of less than 1 nm were easily observable. The *in-situ* spatial resolution of the DIM technique was determined via examination of a dynamically compacted Al-1at%Ta alloy that contained intermetallic precipitates up to 20 microns in diameter. Despite the high degree of surface roughness on these samples, precipitates were located and qualitatively analyzed. The precipitates were observed to form a thinner passive film as a function of applied potential than the matrix material. The incompatibility between the film over the precipitate and that over the matrix may effect the pitting behavior of the alloys.

Acknowledgments:

This research was supported by the Office of Naval Research Contract # N00014-89-J-1180. The authors are grateful to Dr. John Sedricks for his role in providing this support. One of the authors (CCS) was supported throughout this work by a National Science Foundation Award. The aluminum tantalum alloy specimens were donated by Martin Marietta Laboratories. Gene Danko is acknowledged for providing the silicon wafer.

References:

[1] R.M.A. Azzam and N.M. Bashara, Ellipsometry and Polarized Light, Elsevier Science Publishers, New York (1987).

[2] J. Kruger, J. Physique 38, Colloque C-5, supplement to No. 11, CS 129-CS 138 (1977).

[3] D.J. Dunlavy, R.B. Hammond and R.K. Ahrenkiel, Los Alamos National Labs Report LA-UR-81-1806, 6p (1981).

[4] K. Sugimoto and S. Matsuda, J. Electrochem. Soc., 130 (12), 2323 (1983).

[5] K. Sugimota, S. Matsuda, Y. Ogiwara and K. Kitamura, J. Electrochem. Soc., 132 (8), 1791 (1985).

[6] M. Erman and J.B. Theetan, Journal of Applied Physics, 60 (3), 859 (1986).

[7] "Auto Gain Ellipsometers," Bulletin EE, Gaertner Scientific Corporation, p. 13.

[8] A.J. Hurd and C.J. Brinker, J. Physique, 49 (6), 1017 (1988).

[9] A.J. Hurd and C.J. Brinker, in Better Ceramics through Chemistry III, Brinker, Clark and Ulrich, Eds., Materials Research Society, (1988).

[10] R.F. Cohn, J.W. Wagner, and J. Kruger, J. Electrochem. Soc., 135 (4), 1033 (1988).

[11] R.F. Cohn, J.W. Wagner, and J. Kruger, Appl. Opt., 27 (22), 4664 (1988).

[12] R.F. Cohn and J.W. Wagner, in "Review of Progress in Quantitative NDE", 8B, D.O. Thompson and D.E. Chimenti, Eds., 1219 (1989).

[13] R.F. Cohn and J.W. Wagner, in "Proceedings of of the Society for Photo-optical Instrument Engineering," 1036, 125 (1989).

[14] R.F. Cohn and J.W. Wagner, Appl. Opt., 28, 3187 (1989).

[15] R.F. Cohn, Appl. Opt., 29 (2), 304 (1990).

[16] R.T. Allemeier and J.W. Wagner, in "Review of Progress in Quantitative NDE, "10A, D.O. Thompson and D.E. Chimenti, Eds., Plenum Press, New York (1990).

[17] R.L. Anderson, "Revealing Microstructures in Metals," Westinghouse Research Laboratories, Scientific Paper 425-C000-CP2 (1961).

[18] G.D. Davis, T.L. Fritz, B.J. Rees, B.A. Shaw, and W.C. Moshier, Martin Marietta Laboratories Annual Report, MML TR 91-10c (1991).

[19] T. Smith, Surf. Sci., 56, 252 (1976).

[20] J. Kruger and P.C.S. Hayfield, in Handbook on Corrosion Testing and Evaluation, W.H. Ailor, Ed., John Wiley & Sons, New York (1971).

[21] F.L. McCrackin, "A Fortran Program for Analysis of Ellipsometer Measurements," NBS Technical Note 479 (1969).

[22] J. Kruger and J.P Calvert, J. Electrochem. Soc., 114 (1), 43 (1967).

[23] M. Nagayama and M. Cohen, J. Electrochem. Soc., 109 (9), 781 (1962).

[24] F.C. Ho and J.L. Ord, J. Electrochem. Soc., 119 (2), 139 (1972).

[25] J.L. Ord and D.J. De Smet, J. Electrochem. Soc., 123 (12), 1876 (1976).

[26] J.S.L. Leach and B.R. Pearson, Corrosion Science, 28 (1), 43 (1988).

[27] G.D. Davis, W.C. Moshier, T.L. Fritz and G.O. Cote, J. Electrochem. Soc., 137 (2), 422 (1990).

[28] G.S. Frankel, M.A. Russak, C.V. Johnes, M. Mirzamaani, and V.A. Brusic, J. Electrochem. Soc., 136 (4), 1243 (1989).

[29] G.D. Davis, W.C. Moshier, T.L. Fritz, G.O. Cote, G.G. Long, and D.R. Black, Martin Marietta Laboratories Annual Report, MML TR 89-12c (1989).

[30] C.C. Streinz, J. Electrochem. Soc., In Press.

[31] B.A Shaw, T.L. Fritz, G.D. Davis and W.C. Mosier, J. Electrochem. Soc., 137 (4), 1317 (1990).

[32] D.G. Muth, J. Vac. Sci. & Tech., 6, 749 (1969).

[33] R.M. Goldstein, R.J. Lederich, and F.W. Leonhard, J. Electrochem. Soc., 117 (4), 503 (1970).

[34] R.T. Foley, Corrosion, 42 (5), 277 (1986).

[35] W.C. Mosier, G.D. Davis, J.S. Ahearn and H.F. Hough, J. Electrochem. Soc., 134 (11), 2677 (1987).

Figure Captions:

Figure 1: Schematic illustration of the PHCSA (polarizer, half wave plate, specimen, compensator, analyzer) DIM setup. Note that the backbone of the setup is similar to the traditional PSCA (polarizer, specimen, compensator, analyzer) configuration.

Figure 2: Sample ellipsogram of silicon wafer with an SiO_2 film that varies in thickness from approximately 30 to 50 nm. The gray scale of the images is directly proportional to Δ and ψ. The scales provide the values for Δ and ψ.

Figure 3: Photomicrograph of aluminum tantalum precipitate in Al-1at%Ta alloy. The dark region around the precipitate is probably a dealloyed region.

Figure 4: Ellipsogram for iron after 5 hours polarization at 500 mV SCE in a borate buffer solution. Note that the grains can be "observed" in the Δ map but not in the ψ map indicating passive film thickness differences from grain to grain.

Figure 5: $-\delta\Delta$ versus log time for the grains labelled 1 & 2 in Figure 4. $-\delta\Delta$ is proportional to film thickness. The growth kinetics for the film over grain 1 are more rapid than that over grain 2. The final thickness of the film over grain 1 is approximately 0.5 nm thicker than the film over grain 2.

Figure 6: Polarization curve for Al-1at%Ta alloy in pH 7.2 borate buffer solution. The increase in current at approximately 1100 mV SCE is the result of O_2 evolution. O_2 evolution occurs on the aluminum tantalum precipitates similar to those shown in Figure 3.

Figure 7: Ellipsogram of Al-1at%Ta alloy at E_{corr} (-980 mV SCE). Note the spatial noise in the Δ and ψ maps that results from the surface roughness of these alloys.

Figure 8: Δ map (left) and polarized light photograph (right) of Al-1at%Ta alloy. The Δ map was computed after polarization at 1200 mV SCE. The photograph was acquired after polarization at 2000 mv SCE which promoted bubble formation over aluminum tantalum precipitates from O_2 evolution. One such bubble is observed. The "dark spot" in the box on the Δ map indicates that the Δ value for the precipitate is less than that for the matrix material.

Figure 9: $(-\delta\Delta)$ versus applied potential for the precipitate and matrix material in the Al-1at%Ta alloy. A thinner passive film over the precipitate at a given applied potential is implied.

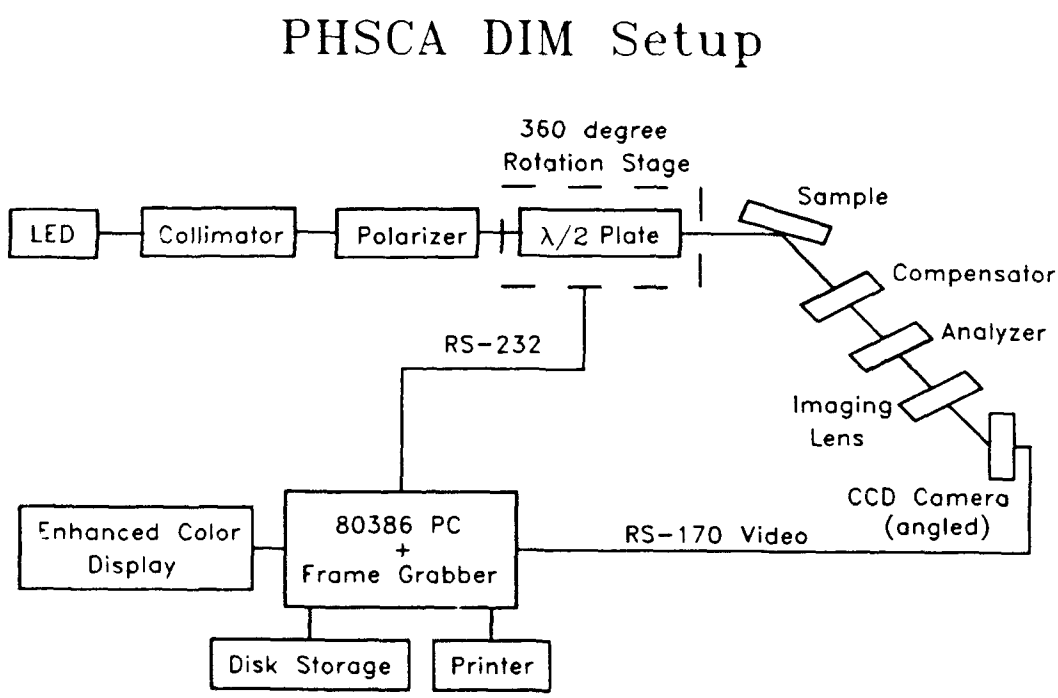

Figure 1: Schematic illustration of the PHCSA (polarizer, half wave plate, specimen, compensator, analyzer) DIM setup. Note that the backbone of the setup is similar to the traditional PSCA (polarizer, specimen, compensator, analyzer) configuration.

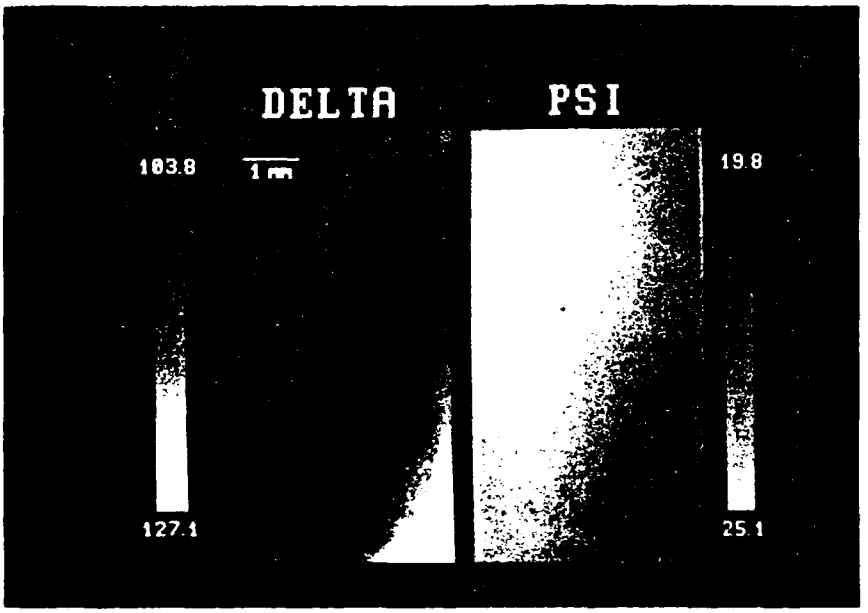

Figure 2: Sample ellipsogram of silicon wafer with an SiO_2 film that varies in thickness from approximately 30 to 50 nm. The gray scale of the images is directly proportional to Δ and ψ. The scales provide the values for Δ and ψ.

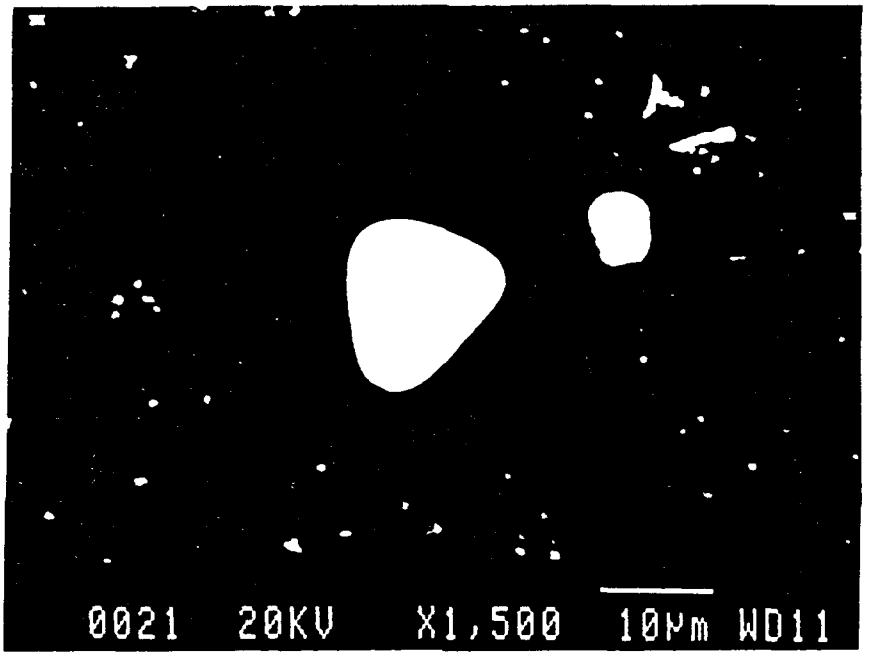

Figure 3: Photomicrograph of aluminum tantalum precipitate in Al-1%Ta alloy. The dark region around the precipitate is probably a dealloyed region.

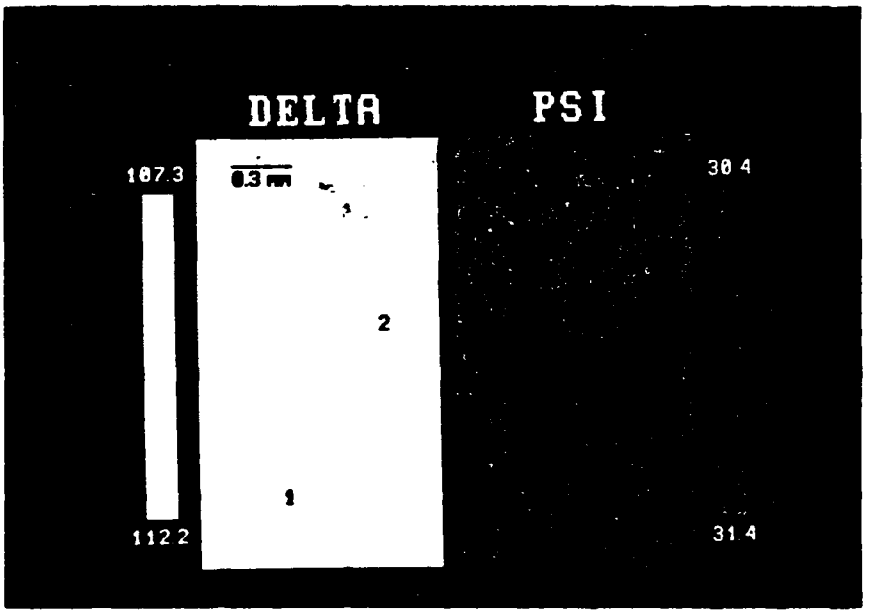

Figure 4: Ellipsogram for iron after 5 hours polarization at 500 mV SCE in a borate buffer solution. Note that the grains can be "observed" in the Δ map but not in the ψ map indicating passive film thickness differences from grain to grain.

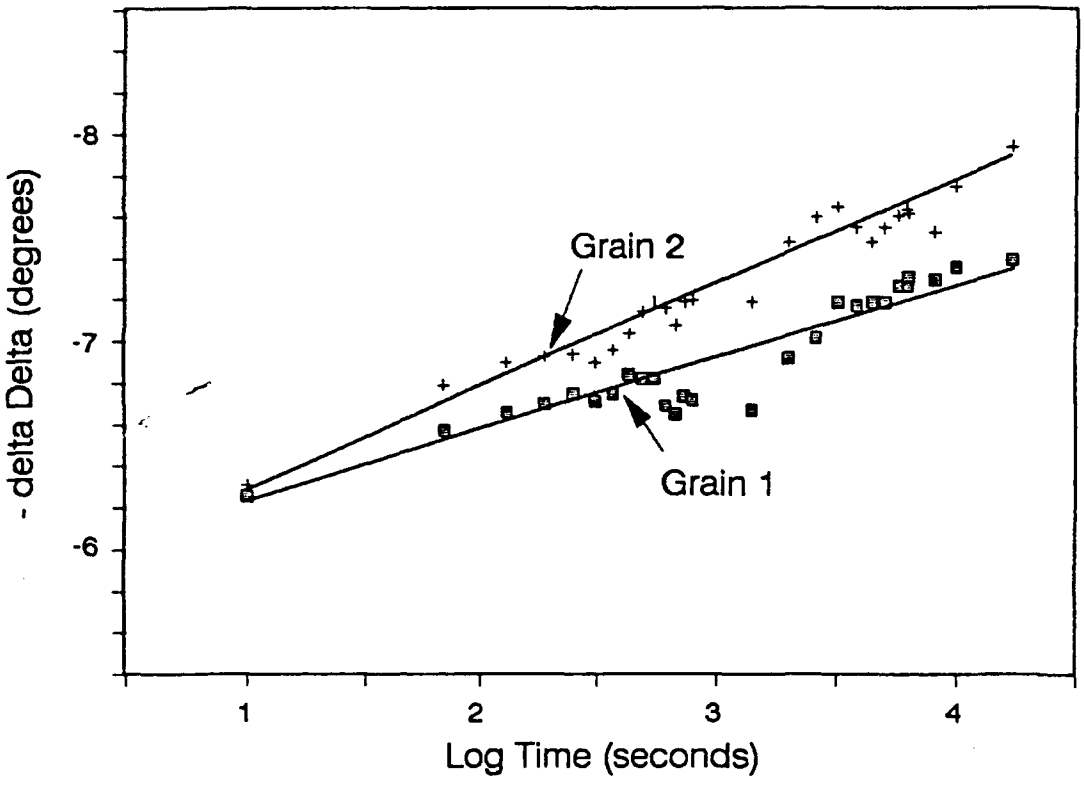

Figure 5: $-\delta\Delta$ versus log time for the grains labelled 1 & 2 in Figure 4. $-\delta\Delta$ is proportional to film thickness. The growth kinetics for the film over grain 2 are more rapid than that over grain 1. The final thickness of the film over grain 2 is approximately 0.5 nm thicker than the film over grain 1.

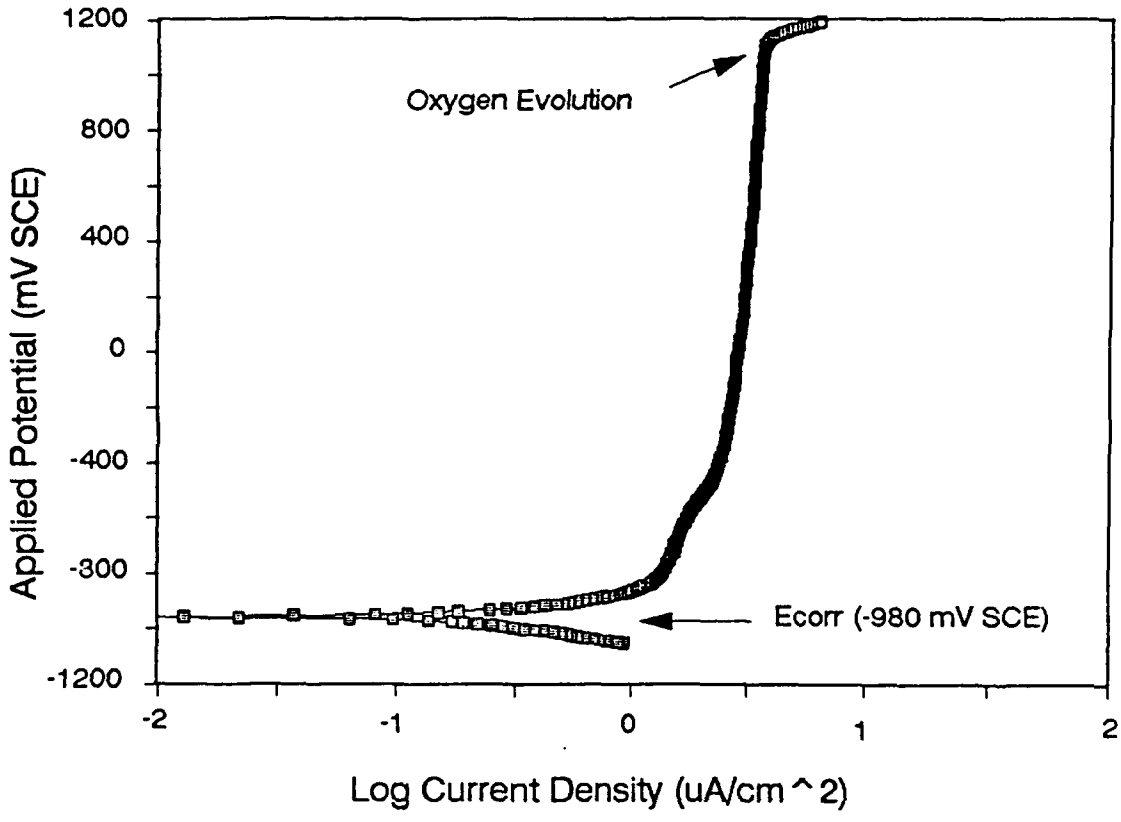

Figure 6: Polarization curve for Al-1%Ta alloy in pH 7.2 borate buffer solution. The increase in current at approximately 1100 mV SCE is the result of O_2 evolution. O_2 evolution occurs on the aluminum tantalum precipitates similar to those shown in Figure 3.

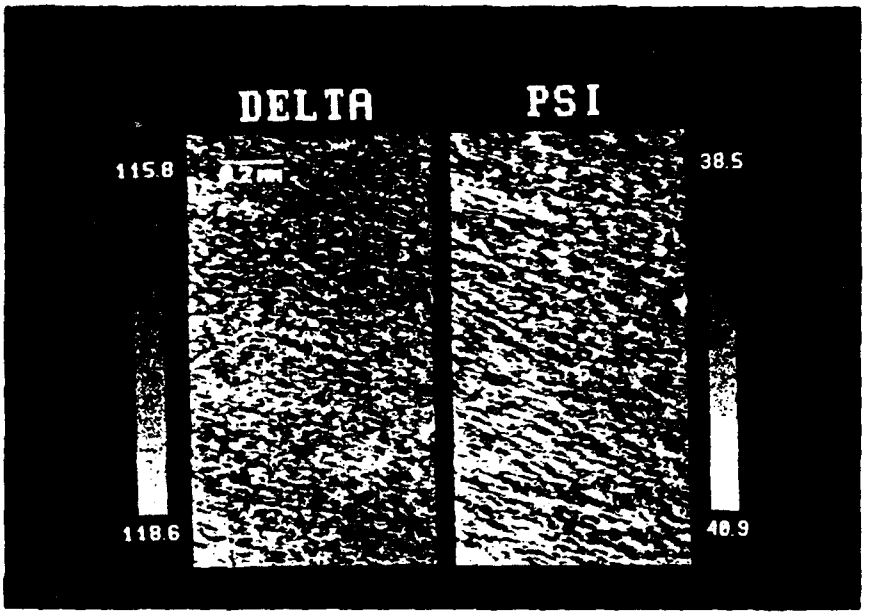

Figure 7: Ellipsogram of Al-1%Ta alloy at E_{corr} (-980 mV SCE). Note the spatial noise in the Δ and ψ maps that results from the surface roughness of these alloys.

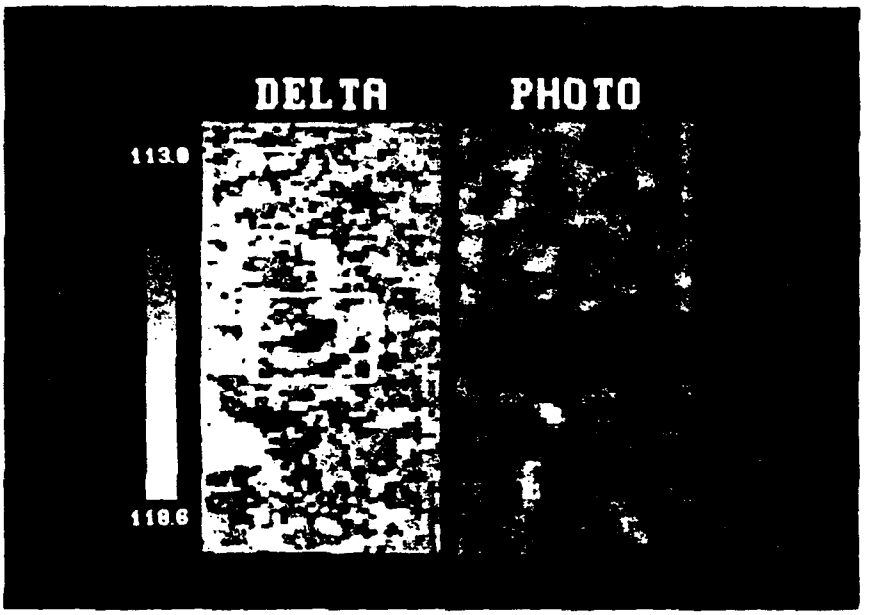

Figure 8: Δ map (left) and polarized light photograph (right) of Al-1%Ta alloy. The Δ map was computed after polarization at 1200 mV SCE. The photograph was acquired after polarization at 2000 mv SCE which promoted bubble formation over aluminum tantalum precipitates from O_2 evolution. One such bubble is observed. The "dark spot" in the box on the Δ map indicates that the Δ value for the precipitate is less than that for the matrix material.

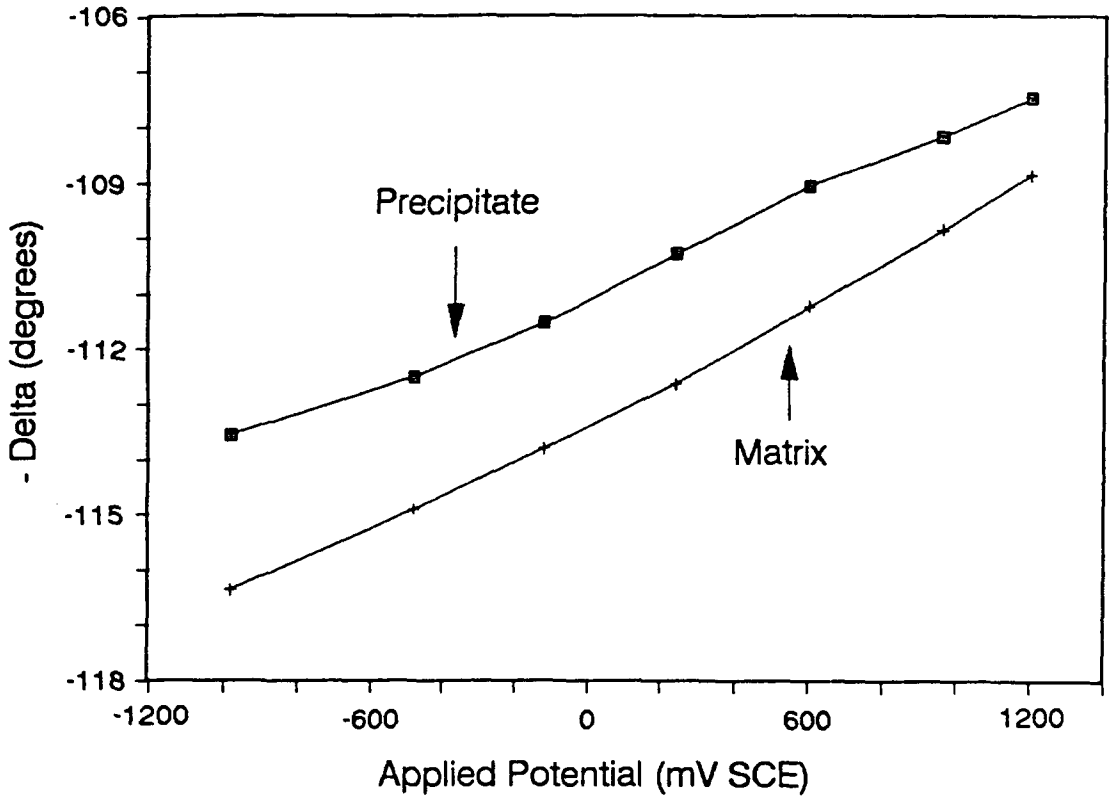

Figure 9: $(-\Delta)$ versus applied potential for the precipitate and matrix material in the Al-1%Ta alloy. The differing slopes indicates that the precipitate forms a thinner passive film at a given potential than the matrix.

APPENDIX 2

A NOVEL METHOD FOR GENERATING QUANTITATIVE LOCAL ELECTROCHEMICAL IMPEDANCE SPECTROSCOPY

R.S. LILLARD[1], P.J. MORAN[2], AND H.S. ISAACS[3]

[1]CORROSION AND ELECTROCHEMISTRY RESEARCH LABORATORY
DEPARTMENT OF MATERIALS SCIENCE AND ENGINEERING
THE JOHNS HOPKINS UNIVERSITY
BALTIMORE, MARYLAND 21218

[2]DEPARTMENT OF MECHANICAL ENGINEERING
UNITED STATES NAVAL ACADEMY
ANNAPOLIS, MARYLAND 21402

[3]DEPARTMENT OF APPLIED SCIENCE
DIVISION OF APPLIED PHYSICS
BROOKHAVEN NATIONAL LABORATORY
UPTON, NEW YORK 11973

Abstract

A Local Electrochemical Impedance Spectroscopy technique (LEIS) for mapping the ac impedance distribution, as a function of frequency, of an electrode has been developed. In LEIS, as in traditional ac impedance methods, a sinusoidal voltage perturbation between the working and reference electrode is maintained by driving an ac current between the working and a distant counter electrode with a potentiostat. Local ac impedances are then derived from the ratio of the applied ac voltage and the local ac solution current density. The local ac current density is obtained from potential difference measurements near the electrode surface using a probe consisting of two micro-electrodes. By measuring the ac potential difference between the micro-electrodes, and knowing their separation distance and, the solution conductivity, the local ac solution current density is derived.

The accuracy of the local ac impedance data generated with this technique was established by investigating two model systems. The first provided a homogeneous electrode which allowed LEIS measurements to be compared to traditional EIS while the second system provided a heterogeneity of know size and location whose components were easily characterized with traditional techniques. It is shown that area normalized scanning ac impedance measurements of the homogeneous electrode agreed well with traditional results. In addition, because LEIS maps the impedance

properties of an electrode, the defect in the heterogeneous electrode was easily detected while traditional ac impedance of this electrode gave little indication of its presence.

Introduction, Background and Approach

AC impedance (also known as Electrochemical Impedance Spectroscopy, EIS) is a powerful non-destructive in situ technique which has been used extensively to investigate electrochemical systems. [1],[2],[3],[4] In the conventional EIS approach, a small sinusoidal voltage perturbation is applied across the electrochemical interface. Impedance data for the whole electrode is then generated by measuring the ratio of the voltage perturbation and its current response as a function of frequency. The impedance is most commonly presented in either Nyquist format ($Z_{imaginary}$ vs Z_{real}) or Bode plots ($|Z| \upsilon s \omega$ and $\theta \upsilon s \omega$). Because, however, the current response of the whole electrode is used to generate impedance data a surface averaged measurement results which can lead to difficulties when interpretating data if the behavior is not uniform over the entire electrode interface; as is the case in localized corrosion systems. The non-uniformity arises because the frequency dependence of the current distribution in the vicinity of a corrosion site is markedly different from that near an inactive, or passive area. [5]

Although EIS has been applied to localized corrosion systems, data analysis for these systems is complex. [6],[7],[8],[9] For this reason, to investigate localized corrosion due to multi-phases, grain boundary effects, or other surface heterogeneities which may occur on an electrode surface a method of generating local ac

impedance data is preferable.

DC Scanning Techniques

Several scanning techniques have been developed for the *in situ* examination of dc currents associated with localized corrosion and surface heterogeneities. The most common being the Scanning Vibrating Electrode Technique (SVET). [10] In SVET a "micro-tip" probe for measuring the current distribution in solution, is constructed from a thin (less then 20 micron) platinum wire and insulated except at the tip. The wire is mounted on a bi-morph piezoelectric reed which vibrates the tip normal to the electrode at a characteristic frequency. For areas on the electrode where there is a net uniform anodic or cathodic current, the dc potential in solution above the electrode will be proportional to distance from the electrode. By oscillating the platinum probe in this potential gradient an induced ac voltage will result. This induced ac signal can be measured precisely with a lock-in amplifier referenced to the oscillation (vibration) frequency of the piezoelectric. The dc current distribution in solution above the electrode has been mapped with this vibrating probe by scanning it at a distance less than 50 microns above the electrode with an X-Y translation stage. [10-14]

While the SVET has been used successfully to investigate the initiation of stress corrosion cracking [11], surface heterogeneities [12] and galvanic corrosion [13],[14], its application is limited to systems which are electrochemically active; ie. dc currents must flow in solution.

Recent attempts to develop scanning ac impedance systems

Isaacs and Kendig [15], as well as other investigators [16],[17], have combined scanning technology with impedance methods in an attempt to generate local ac impedance data for discrete areas on electrodes.

In these techniques, the electrode to be examined was polarized locally with a small disc shaped probe that contained "micro" reference and counter electrodes. In an attempt to confine the current generated by the local polarization to the area of interest, a thin layer cell geometry was employed. This was accomplished by maintaining a distance of 30 microns between the disc shaped probe and electrode surface. While this technique has been used to generate qualitative results, no quantitative local ac impedance data has been produced with this method. In addition, the use of a thin layer cell geometry, may markedly influence the natural corrosion process, by altering mass transport for example. The thin layer cell's effectiveness in confining the current density distribution to the local area also depends vastly on the impedance properties of the electrode.

A novel method of generating local ac impedance data

This paper presents a novel method for generating quantitative local ac impedance. The technique is founded on the premiss that the ac solution current densities *very* near the working electrode, in a conventional three electrode ac impedance measurement, are proportional to the local impedance properties of the electrode.

Other investigators have demonstrated that the current distribution very near an electrode may be mapped in three dimension; each, or any combination of which may be mapped for an electrode surface by choosing the correct probe geometry. [18],[19],[20] To simplify data analysis, this study has chosen to only measure the component of the ac current normal to the electrode. Because current and potential lines are perpendicular to one another, to measure the ac solution current density normal to the electrode it is necessary to measure the ac potential drop between planes parallel to the electrode. Further, to effectively map the local impedance properties of an electrode this ac potential drop measurement must be made on a relatively small scale. To accomplish this the two electrode micro-probe shown in Figure 1 was designed.

To obtain the local ac solution current density at the tip of the probe, first the ac potential difference between the two probe electrodes is measured with a frequency response analyzer or lock-in analyzer. The ac solution current density at the probe tip is obtained from this potential measurement by using the the following relationship which is derived from Ohm's law:

$$i(\omega)_{local} = \frac{\Delta V(\omega)_{probe} \cdot \sigma}{l} \qquad \text{Eq.(1)}$$

where:

$i(\omega)_{local}$: the local ac solution current density

$\Delta V(\omega)_{probe}$: ac potential difference at the probe

σ: solution conductivity

l: separation distance between the tip "micro-openings"

in units of amps/cm^2, volts, (ohm cm)$^{-1}$, and cm respectively. The magnitude of the local impedance is derived from Equation 1:

Eq.(2)

$$|Z(\omega)|_{local} = \frac{V(\omega)_{applied}}{\Delta V(\omega)_{probe}} \cdot \frac{l}{\sigma}$$

where:

$V(\omega)_{applied}$: magnitude of the applied voltage perturbation between the reference and working electrodes.

which is an area normalized local impedance value, in units of ohm cm^2. It should be noted in the derivation of $|Z(\omega)|_{local}$ that the ac solution current density at the probe tip (Eq. 1) is assumed to be equal to the current density at the electrode surface; ie all of the ac current at the tip is assumed to be traveling normal to the electrode. The validity and implications of this assumption shall be addressed in the discussion section of this paper.

Experimental

Probe design

The bi-electrode probe used in these experiments to measure the component of the ac solution density normal to the electrode shown in Figure 1a & 1b. It was constructed by drawing down two parallel and attached glass capillaries with an initial inside diameter of 1.0 mm, to a final inside diameter of approximately 0.10 mm. As shown in Figure 1, these "micro-openings" were displaced (with respect to the plane of the electrode) both vertically and horizontally by 0.80 +/- 0.050 and 0.30 +/- 0.050 mm respectively. Into each of these glass tubes, a thin platinum wire, approximately 0.225 mm in diameter, was inserted. To reduce the interfacial impedance of these platinum electrodes, each wire was platinized by cathodic polarization in 2% chloroplatinic acid at a density of approximately 100 mA/cm^2 for approximately 5 minutes. [21] To measure the normal component of the current, this probe was held at approximately an 80 +/- 1 degree angle with respect to the electrode so that the openings would be aligned normal to the electrode; along the Z axis. This configuration, shown in Figure 1b, provided a final probe separation distance along the Z axis of approximately 0.9 mm.

Electrochemical and Scanning Apparatus

A Solartron 1286 Electrochemical Interface was used to control the dc potential of the test electrodes and apply the ac sinusoidal voltage perturbation generated by a Solartron 1255 Frequency Response Analyzer (FRA). Because the

probe impedances were high relative to the input impedance of the FRA (approximately 3×10^5 ohms *versus* 1×10^6 ohms respectively) direct measurement of the probe signal with the Solartron 1255 FRA resulted in an attenuation of true potential difference between the probe electrodes. In addition, an impedance mismatch between the two electrodes created a high common mode voltage at the probe electrode. The combination of these two effects prevented accurate measurement of the ac potential difference between the probe electrodes when made directly with the Solartron FRA.

To overcome these problems, the probe signal was first buffered with a high input impedance, high common mode rejection ratio and low output impedance (1×10^9 ohms, 1×10^6 and <1 ohm respectively) Analog Devices AD-625 linear output instrumentation amplifier. The instrumentation amplifier also permitted the input signal to be amplified by as much as 1000x, allowing very small potential differences between the probe electrodes to be easily measured with the Solartron FRA. Further information on this instrumentation is available elsewhere.[19]

To generate ac impedance maps of electrodes with the probe, a high resolution, a high accuracy scanning system was assembled. To avoid unnecessary vibration of the probe, which may have resulted in an error in the measurements, the scanning system was designed to move the electrode, in a specially designed cell, below the probe which was held stationery. Movement of the cell in the X and Y directions was accomplished by mounting two Aerotech ATS210 *Accudex*

stages orthogonoly to one another. Each of these stages were driven by Aerotech 101SM-DM4005 stepper motors. This scanning system has a resolution of 1 micron and an accuracy of 2.5 microns / 25 mm.

Because it is somewhat impractical to manually control the FRA, potentiostat, and motion controller while simultaneously recording data during an experiment, a computer data acquisition system and the necessary software was developed and is discussed in detail elsewhere. [19]

Model electrodes, and experimental parameters

To demonstrate the validity of the experimental method a homogeneous, or uniform, electrode surface consisting of a single phase high purity material was first tested in an electrolyte which did not produce localized corrosion. The electrode for thisexperiment, presented in Figure 2a, was a 2.25 cm diameter 99.999% aluminum cylinder mounted in epoxy and was studied in a 0.5M boric acid/0.05M sodium borate buffer solution (pH = 7.2, $\sigma = 5.32 \times 10^{-3}\ ohm^{-1} \cdot cm^{-1}$) to keep it free of localized corrosion.

To demonstrate that the technique was sensitive to surface heterogeneities a second electrode was designed. The electrode was constructed by force molding a 99.999% pure aluminum sample around a 0.127 cm diameter molybdenum wire. The final outside diameter of the electrode being 1.27 cm. This electrode was mounted in epoxy and a diagram of it is presented in Figure 2b.

In all scanning ac impedance measurements, a 30 mV rms sinusoidal voltage perturbation was potentiostatically maintained between the test electrode and a saturated calomel reference electrode. An applied dc potential of -0.675V vs SCE was also maintained between the test and reference electrodes. For the Al/Mo electrode this dc potential is approximately 100 mV cathodic to E_{corr} while for the 99.999% Al electrode this dc potential was approximately 35 mv anodic to E_{corr}. Impedance maps were generated for the Al/Mo electrode in the frequencies range of 4.64 to 4677 Hz while for the 99.999% Al electrode ac impedance maps were generated over a frequency range of 2.51 to 6310 Hz.

Because each electrode was symmetric about its center it was only necessary to map a small section of each, as presented in Figures 2a and 2b. For the Al/Mo electrode this area was approximately 0.65 cm^2 (1.47 cm x 0.44 cm) and was mapped by stepping the electrode below the probe in the X and Y directions in increments of 0.070 and 0.040 cm respectively. The scan area of the 99.999% Al electrode was approximately 0.11 cm^2 (0.33 cm x 0.33 cm) and was mapped by stepping the electrode below the probe in the X and Y directions in increments of .030 and .030 cm.

To evaluate the scanning ac impedance measurements, traditional ac impedance experiments were performed on the Al/Mo electrode and 99.999% Al electrodes used in the scanning experiments as well as on a 99.95% molybdenum electrode. These experiments were also carried out in the same boric acid/sodium

borate buffer solution and at the same applied dc potential (-0.675V vs SCE) and were conducted with a Princeton Applied Research Electrochemical Impedance System and 378 Software. The ac voltage perturbation used for these experiments was 10 mV rms and 5 data points per decade of frequency were recorded over a frequency range of $1x10^{-3}$ to $1x10^{5}$ hertz.

Prior to all impedance experiments each electrode surface was first polished with successively finer grits of silicon carbide paper finishing with 4000 grit. The surfaces were then further polished on a polishing wheel with diamond spray, the final grit size being 1 micron. After polishing, the sample was washed and then degreased with methanol and ethanol and left in the laboratory air for periods between 6 and 24 hours before immersion in the test solution.

Results

Traditional ac impedance experiments

Before analyzing the ac impedance maps of the 99.999% aluminum and aluminum / molybdenum electrodes, it will be helpful to first examine the data from traditional ac experiments performed on the aluminum, molybdenum, and the Al/Mo electrodes. The results of theses experiments are presented in the form of Bode Magnitude and Bode Phase plots in Figures 3a and 3b respectively for later reference. It may be noted that some of the low frequency data in these plots, below 10^{-1} hertz, appears noisy or irreproducable. This, however, will have little consequence on our discussion.

Scanning ac impedance maps

The aluminum electrode

Figure 4 presents a contour map of the magnitude of the impedance, $|Z|$, of the Al electrode at 6310 hertz for the scan area presented in Figure 2a. This figure clearly shows a radial distribution in the impedance over the aluminum electrode; the maximum impedance value occurring near the center of the electrode. A profile of this distribution, $r\,vs\,|Z|$, is presented in Figure 5. The ac current distribution which corresponds to the impedance distribution, easily obtained from Ohm's law, is also presented in Figure 5. This ac current distri-

bution is, as expected at high frequencies, similar in contour to the well known static primary current distribution for a disc electrode in an infinitely insulating plane. [22] [23]

From the contour map presented in Figure 4 an estimation of the sensitivity of this technique can be made. The percent difference in the local ac solution current density, i_{local}, between any two adjacent points which is discernable by the probe is given by:

$$sensitivity = \frac{i_{local,1} - i_{local,2}}{i_{total}} \cdot 100 \qquad \text{Eq.(3)}$$

The ac current density at the electrode, i_{total}, was derived from an estimation of the average interfacial impedance from Figure 4 and Ohm's Law while the local ac solution current density for two adjacent points, $i_{local,1}$ and $i_{local,2}$, was obtained from there impedance values (Equations 1 and 2). In this manner the sensitivity of the technique to changes in the ac solution current density is estimated from Equation 3 to be 0.13%.

Presented in Figure 6 are two Bode Magnitude Plots generated from scanning impedance measurements. These curves were made by plotting the impedance values for the two locations in Figure 4 marked points X1 and X2 as a function of frequency. A comparison between the Bode Magnitude Plots for the Al electrode obtained from the scanning ac impedance technique (Fig. 6)

and those obtained from traditional ac impedance techniques (Fig. 3a) is presented in Figure 7. Using standard least squares methods [24], the impedance values from the two techniques are found to agree within 1.6% +/- 1.5% over the frequency range in which scanning ac impedance maps were generated.

The aluminum / molybdenum electrode

Representative ac impedance maps of the aluminum / molybdenum electrode at 4677 and 4.7 hertz are presented in Figures 8a and 8b respectively for the scan area shown in Figure 2b. Inspection of these maps reveals that at low perturbation frequencies the local impedance of the molybdenum is less than the impedance of the aluminum. At high perturbation frequencies the impedance of the electrode becomes more and more uniform as the interfacial impedance "shorts out"; ie the frequency of the ac current is high enough such that it may be capacitatively passed across the electrode interface with virtually no impedance.

Figure 9 presents Bode Magnitude plots for the aluminum and molybdenum areas of the Al/Mo electrode generated from scanning ac impedance data. Each curve in this figure illustrates the behavior of the magnitude of the impedance for one discrete location, either over the molybdenum or aluminum portion of the Al/Mo electrode, as a function of frequency. It may be noted that in Figure 9, in the frequency range between 100 an 6000 hertz, a dip in the magnitude of the Mo impedance data may be seen. This "dip" at high frequency may also be

observed on close inspection of the Bode magnitude data for 99.999% Al obtained from the scanning ac impedance technique. While this anomaly is not wholly understood at this time it has had little consequence on data analysis.

A comparison between the Bode Magnitude Plots for the aluminum electrode obtained from traditional ac impedance techniques (Figure 3a) and the impedance of the aluminum portion of the aluminum / molybdenum electrode obtained from the scanning ac impedance technique (Figure 9) is presented in Figure 10. As expected, the magnitude of the impedance of the aluminum portion of the Al/Mo electrode agrees well with the traditional ac impedance data for pure aluminum measured under the same experimental conditions. A similar comparison of scanning data from the molybdenum portion of the electrode also shows good agreement with traditional experiments except in the region of the "dip" discussed above.

Discussion

The spatial resolution of this technique is limited, in part, by the size of the probe tip; ie the probe will only be able to resolve (spatially) defects which are of the same size as the probe or larger. If the size of the probe is decreased to resolve smaller and smaller objects, however, the impedance of the probe will increase proportionally. This increase in probe impedance causes a corresponding decrease in the probe's ability to accurately measure the ac solution current density. [19] Ideally these two competing effects should be optimized. In this study the size of the electrodes, Al and Mo wire, were relatively large which allowed a probe size to be used whose impedance could be easily compensated for with readily available high impedance circuitry.

Another factor which controls the resolution of this technique is the probe / electrode separation distance. It is well known that the solution current density for these cell geometries is a function of distance from the electrode surface; ie. the ac current tends to "spread" in solution as function of distance from the electrode. [22],[23] Although $|Z|$ maps were generated for large areas of the electrode, this "spreading" effect was taken into account when the data was examined and, as a result, Bode magnitude plots were generated from LEIS data only for points on the electrode surface where the impedance data from point to point was relatively uniform or "flat". In these regions the differential probe voltage was assumed to result from a normal ac current travelling up from the electrode through a solution volume

whose cross sectional area was defined by one grid element (the X and Y step sizes). For these areas a value for the local impedance was then derived from Equation #2 as discussed in the background section of this paper.

The data in Figure 7, the comparison of traditional and LEIS Bode magnitude data from the aluminum electrode, is a clear indication that this approach is valid. As discussed, the largest deviation of the LEIS data from traditional data in this figure is approximately 5% which indicates that in regions where the impedance data is fairly "flat" the ac solution current density at the probe tip is a good approximation of the ac current density at the electrode. Further, this argument is also supported by the data presented in Figure 10, the comparison of Bode magnitude data obtained with traditional techniques for the Al electrode and that obtained with LEIS for the aluminum portion of the Al/Mo electrode.

As a result of this assumption, there can be an error in the local impedance measurement if the cell volume is influence by current travelling diagonal to the electrode. Such an error is seen by closely examining Figures 8a and 8b, the impedance map of the Al/Mo electrode at 4677 Hz and 4.7 Hz respectively. The molybdenum "defect" in the 4.7 Hz map appears to be approximately 3.0 mm in diameter, while in the map at 4677 Hz map it appears to be approximately 1.88 mm. The true diameter of the wire is 1.27 mm. This effect is observed because not all of the ac current in the region over the aluminum near the molybdenum wire is travelling normal to the electrode. The differential probe voltage in this region is effected by both the ac current from the aluminum portion of the electrode directly below the probe trav-

elling normal to the electrode and the normal component of the current travelling diagonally (outward) from the Mo wire. The consequence of this additional ac current from the Mo wire is that the impedance of the aluminum in the region near the Mo wire appears to be smaller than it truly is or, conversely, the Mo defect appears larger than it truly is. The end result is that if a Bode magnitude plot for aluminum were to be generated from LEIS taken in this region near the Mo wire it would surely be in error. To obtain a true, normalized local impedance deconvolution of the impedance maps is necessary. [13] Addressing this procedure is, however, beyond the scope of this paper.

Conclusions

A Local Electrochemical Impedance Spectroscopy (LEIS) system for generating local ac impedance data has been developed. In this system, as in traditional ac impedance methods, a sinusoidal voltage perturbation between the working and reference electrodes is maintained by driving an ac current between the working and a distant counter electrodes. Local ac impedances are derived from the ratio of the applied ac voltage perturbation to the local ac solution current densities. The ac solution current density at any given *discrete* site above the electrode is obtained from potential difference measurements near the electrode surface using a probe consisting of two micro-electrodes. By measuring the ac potential difference between the micro-electrodes, and knowledge of both the separation distance between the probe electrodes and the solution conductivity, the local ac solution current density is derived. The ac impedance properties, at each frequency of interest, of an electrode are mapped in this system, by scanning this probe across the electrode surface with high resolution X-Y translation stages.

The accuracy of the data generated with the scanning ac impedance system has been demonstrated by investigating a homogeneous 99.999% aluminum electrode system and a heterogeneous molybdenum / aluminum electrode system with Local Electrochemical Impedance Spectroscopy as well as with traditional ac impedance techniques. Comparison of the Bode Magnitude plot generated with LEIS for the 99.999% aluminum electrode system with the Bode Magnitude plot generated with

List of Figures

Figure 6 Bode Magnitude plots from LEIS measurements on the aluminum electrode. The (square) is from position X-1 in Figure 4 while the (plus) is from position X-2 .

Figure 7 A comparison of the Bode Magnitude data for the aluminum electrode generated from LEIS measurements (plus) and traditional EIS (diamond).

Figure 8 3-D maps of the magnitude of the impedance for the aluminum / molybdenum electrode generated with LEIS at **a)** 4677 hertz **b)** 4.7 hertz.

Figure 9 Bode Magnitude plots from LEIS data for the aluminum / molybdenum electrode. The (square) is from one position over the aluminum while the (triangle) is from one position over the molybdenum.

Figure 10 A comparison of the Bode Magnitude data from bulk aluminum (diamond) and one position over the aluminum portion of the Al/Mo electrode (square).

References

1. Macdonald, J.R., ed., Impedance Spectroscopy, (New York: Wiley, 1987).

2. Epelboin, I., Gabrielli, C., Keddam, M., and Takenouti, H., "Alternating-Current Impedance Measurements Applied to Corrosion and Corrosion Rate Determination", in: Electrochemical Corrosion Testing, ASTM STP 727, F. Mansfeld and U. Bertocci eds., ASTM, 1981, pp 150-166.

3. Macdonald, D. D., and McKubre, M. C. H., "Electrochemical Impedance Techniques in Corrosion Science," Electrochemical Corrosion Testing, ASTM STP 727, F. Mansfeld and U. Bertocci eds., ASTM, 1981, pp. 110-149.

4. Kelly, R.G., Moran, P.J., "The Rate Limiting Mechanism in Li/I_2 (P2VP) Batteries; II Effect of Discharge Rate on the Contributions of the cell Components to the Cell Impedance", **The Journal of the Electrochemical Society**, vol. 134, no. 1, 1987.

5. McKubre, M.C.H., "Techniques for AC Impedance Measurements in Corrosion Systems", paper # 480, NACE, Corrosion 87, San Francisco Ca., March 1987.

6. Kendig, M. W., and Mansfeld, F., "AC Electrochemical Impedance of a Model Pit", **Proc. Fall Meeting of the Electrochemical Soc.**, Vol. 82-2, pp 105-6, 1982.

7. Oltra, R., Keddam, M., "Application of Impedance Technique to Localized Corrosion", **Corrosion Science**, Vol. 28, No. 1, pp. 1-18. 1988.

8. Juttner, K., Lorenz, W. J., Kendig, M. W., Mansfeld, F., "Electrochemical Impedance Spectroscopy on 3-D Inhomogeneous Surfaces, "Journal of the Electrochemical Society, Vol. 135, No. 2, pp. 332-39, 1988.

9. Hitzig, J., Juttner, K., Lorenz, W. J., "AC-Impedance Measurements on Corroded Porous Aluminum Oxide Films", **Journal of the Electrochemical Society**, Vol. 133, No. 5, pp. 887-892, 1986.

10. Jaffe, L.F., and Nuticelli, R., Journal of Cell Biology, vol 63, pg 614, 1974.

11. Isaacs, H.S., "The Initiation of Stress Corrosion Cracking of Sensitized Type 304 Stainless Steel in Dilute Thiosulfate Solution", **The Journal of the Electrochemical Society**, vol. 135, no. 9, 1988.

12. Isaacs, H., S., "The Use of the Scanning Vibrating Electrode Technique to detect Defects in Ion-Vapor Deposited Aluminum in Steel", **Corrosion**, Vol. 43, pp. 594-98, 1987.

13. Isaacs, H. S., "The Measurement of Soldered Copper Using the Scanning Vibrating Electrode Technique", **Corrosion Science**, Vol. 28, No. 6, pp. 547-58, 1988.

14. Crowe, C. R., and Kasper, R. G., "Ionic Densities in the Nearfield of a Iron-Copper Galvanic Couple", **The Journal of the Electrochemical Society**, Vol. 133, No. 5, pp. 879-87, 1986.

15. Isaacs, H. S., and Kendig, M. W., "The Determination of Surface Inhomogeneities Using a Scanning Probe Impedance Technique", **Corrosion**, Vol. 36, pp. 269-74, 1980.

16. Hughes, M. C., and Parks, J. M., "An Ac Impedance Probe as an Indicator of Corrosion and Defects in Polymer/Metal Substrate Systems", in Corrosion Control by Organic Coatings, H. Leidheiser Jr. ed., NACE, Houston TX, 1981.

17. Standish, J.V., Leidheiser Jr., H., "The Electrical Properties of organic Coatings On a Local Scale-Relationship to Corrosion", **Corrosion**, vol 36, no. 8, NACE, 1980.

18. Isaacs, H.S., Ishikawa, Y., The Application of the vibrating probe to Localized Corrosion", in Electrochemical Techniques for Corrosion Engineering, R Baboian ed., NACE, pg. 17,1986.

19. Lillard, R.S., "A Novel Method for Generating Local Electrochemical Impedance Spectroscopy", MSE essay, Department of Materials Science and Engineering, The Johns Hopkins University, Baltimore, Maryland, 1990.

20. Scheffey, C., "Two Approaches to Construction of Vibrating Probes for Electrical Current Measurement in Solution", **Review of Scientific Instrumentation**, vol. 59, no. 5, pg 787, 1988.

21. Interfacial Electrochemistry, an Experimental Approach, E. Gileadi, E. Kirowa-Eisner, J. Penciner, Addison-Wesley, Massachusetts, 1975, pp 216-18.

22. Newman, J.S., Electrochemical Systems, Prentice-Hall, Englewood, NJ, 1973.

23. Nanis, L., Kesselman, W., "Engineering Applications of Current and Potential Distributions in Disk Electrode Systems", The Journal of the Electrochemical Society, vol. 118, no. 3, 1971.

24. Bevington, P.R., Data Reduction and Error Analysis for Physical Sciences, McGraw-Hill, New York, 1969.

25. Tokuda, K., Gueshi, T., Aoki, K., Matusuda, H., **The Journal of the Electrochemical Society**, Vol 132, No. 10, pg. 2390-98, 1985.

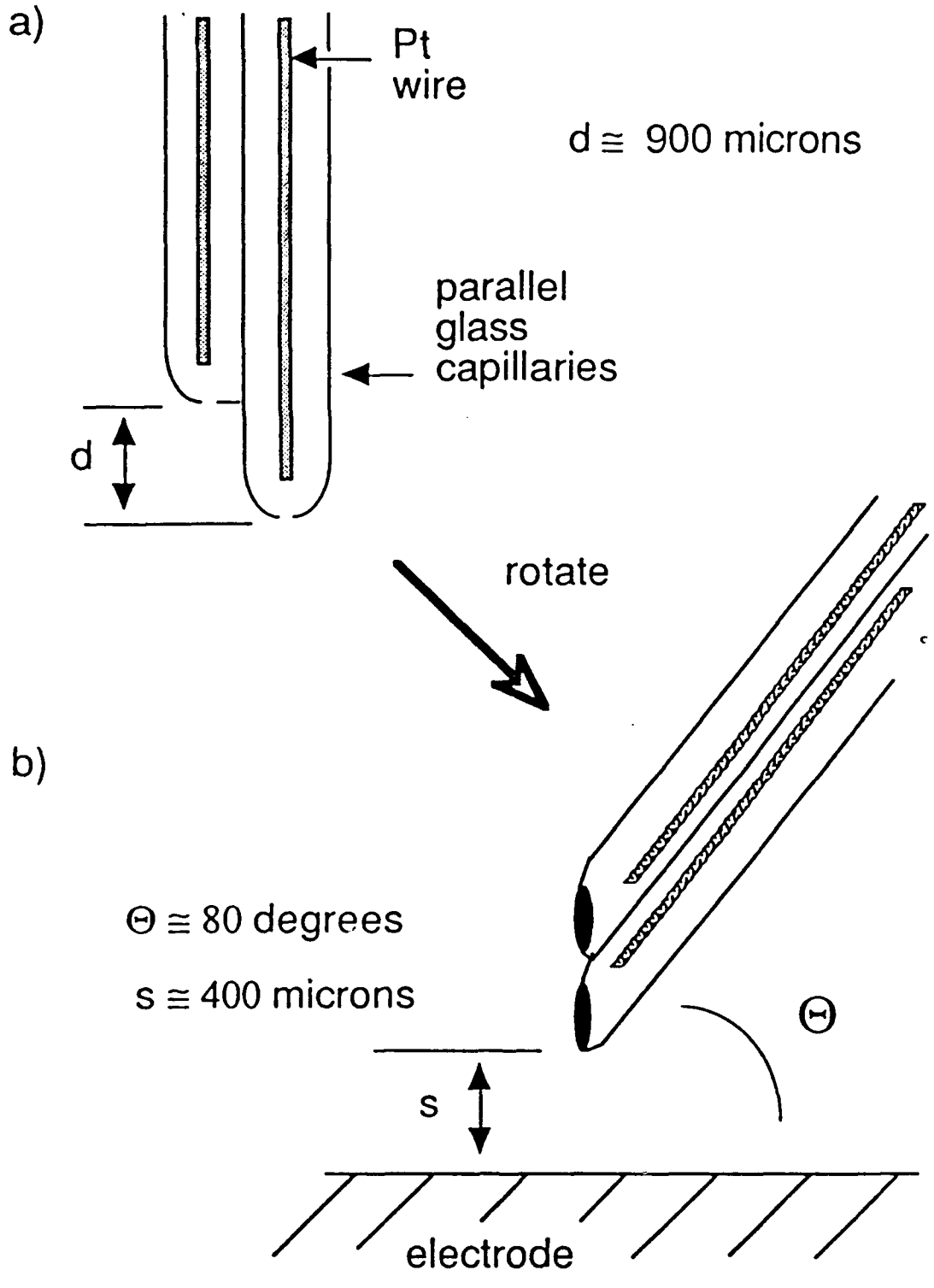

Figure 1 A diagram of the bi-electrode probe used to make local ac impedance measurements.

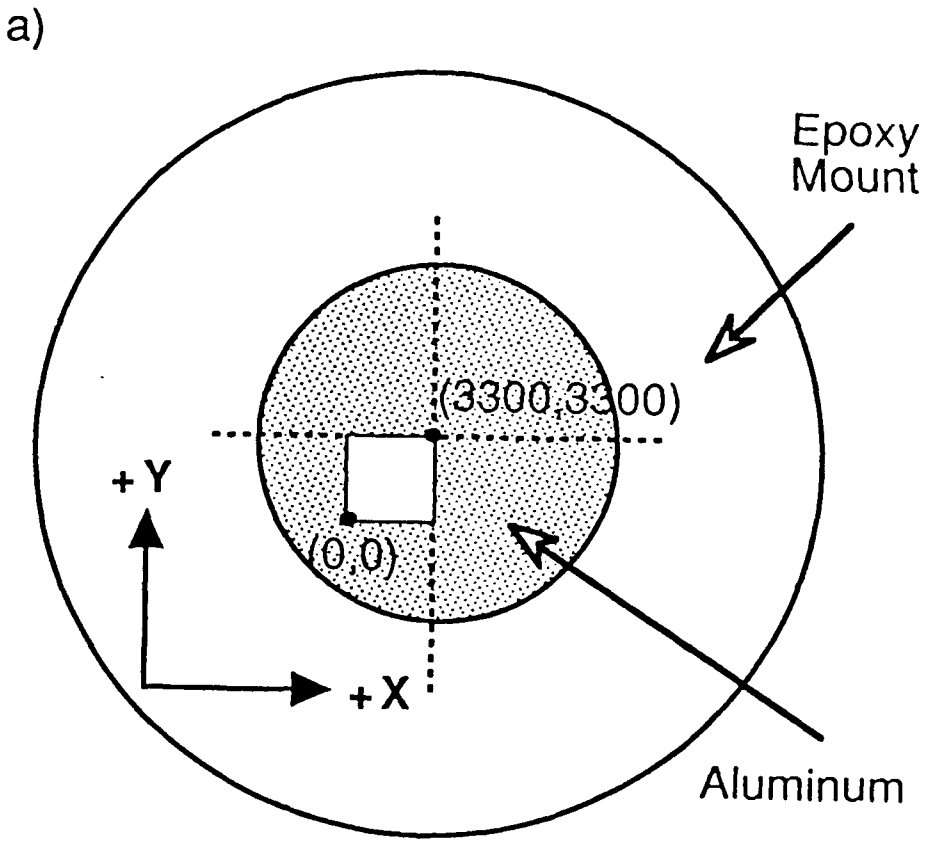

Figure 2 Diagrams of the model electrodes examined with including the area examined with the scanning EIS technique **a)** the aluminum electrode **b)** the aluminum / molybdenum electrode.

b)

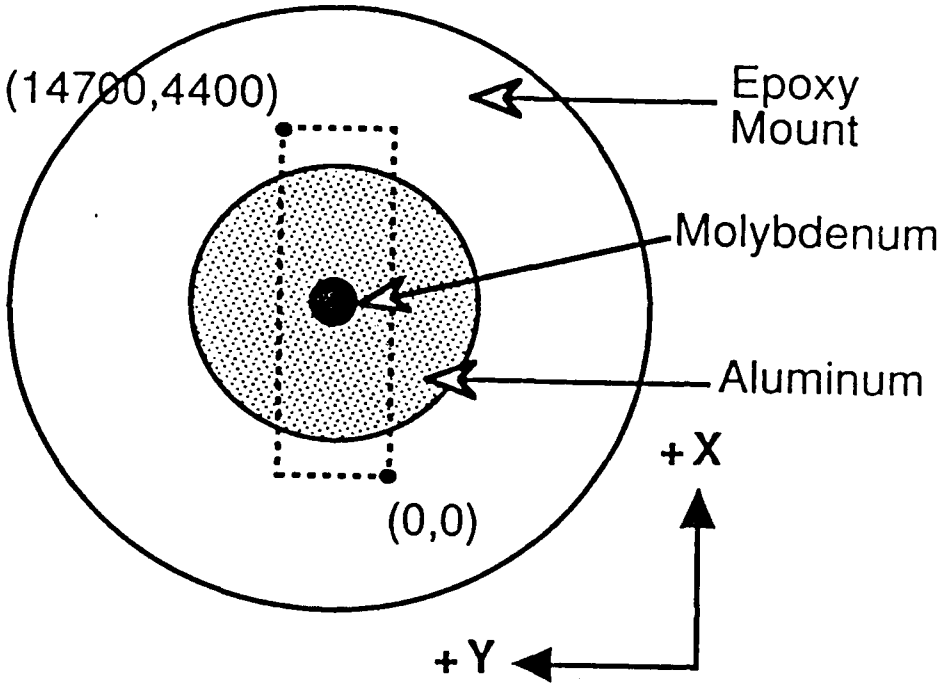

Fig 26

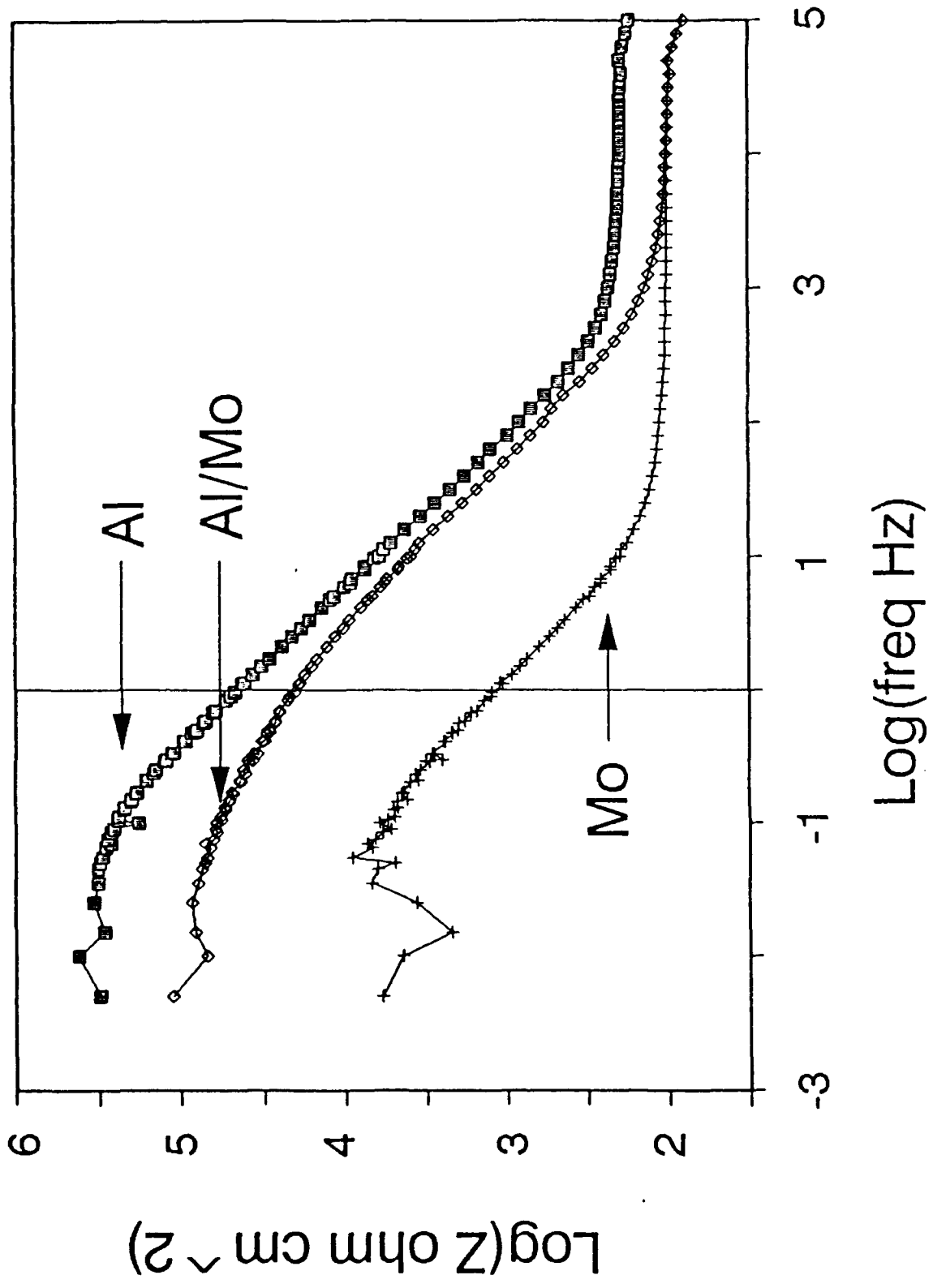

Figure 3 Traditional EIS data for bulk aluminum, bulk molybdenum, and aluminum / molybdenum electrodes **a)** Bode Magnitude Plot **b)** Bode Phase Plot.

Fig 3b

Figure 4 A map of the magnitude of the impedance (in contour) of the aluminum electrode at 6310 hertz generated with the scanning impedance technique. Each contour line represents 1.0 ohm cm^2.

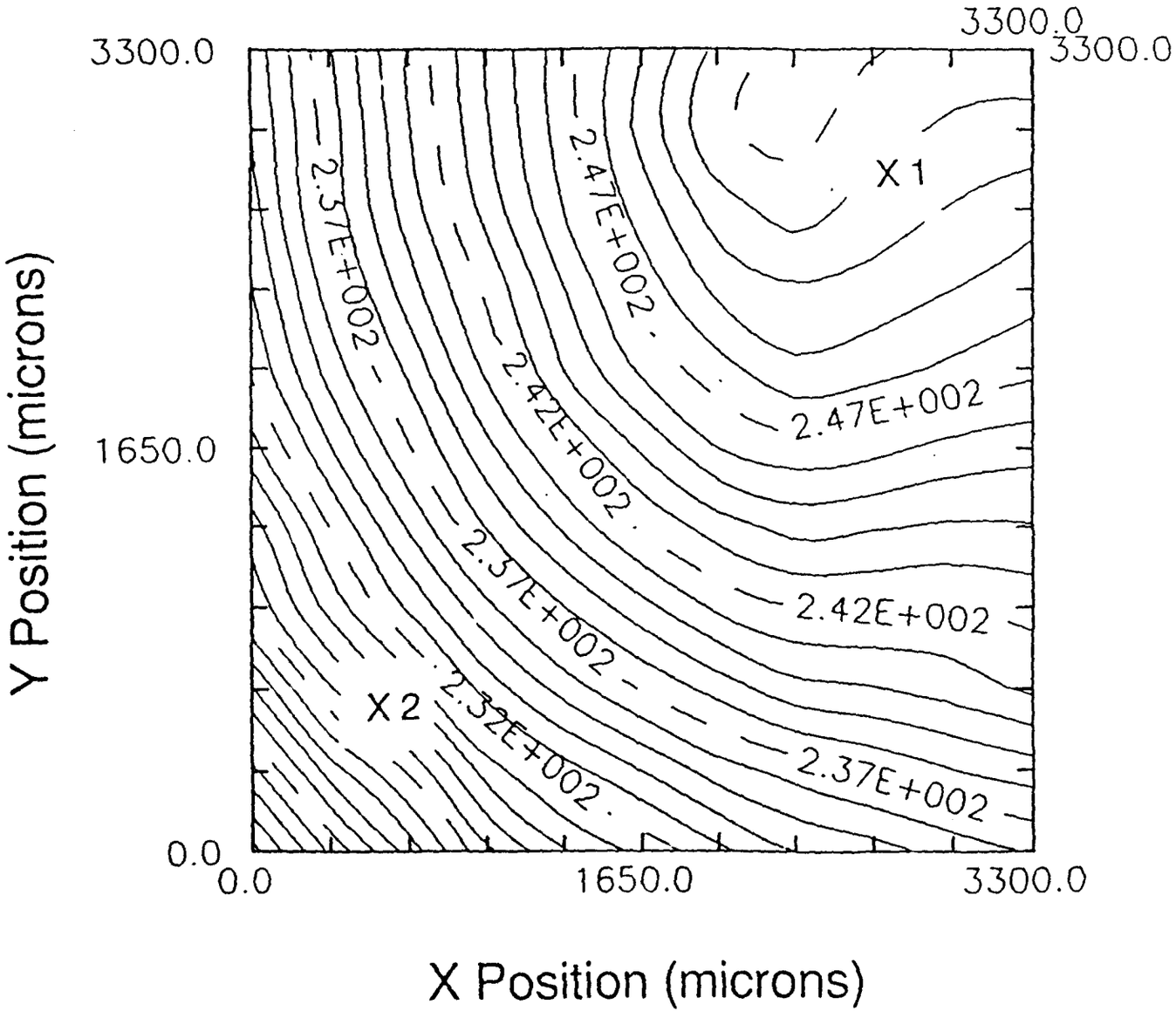

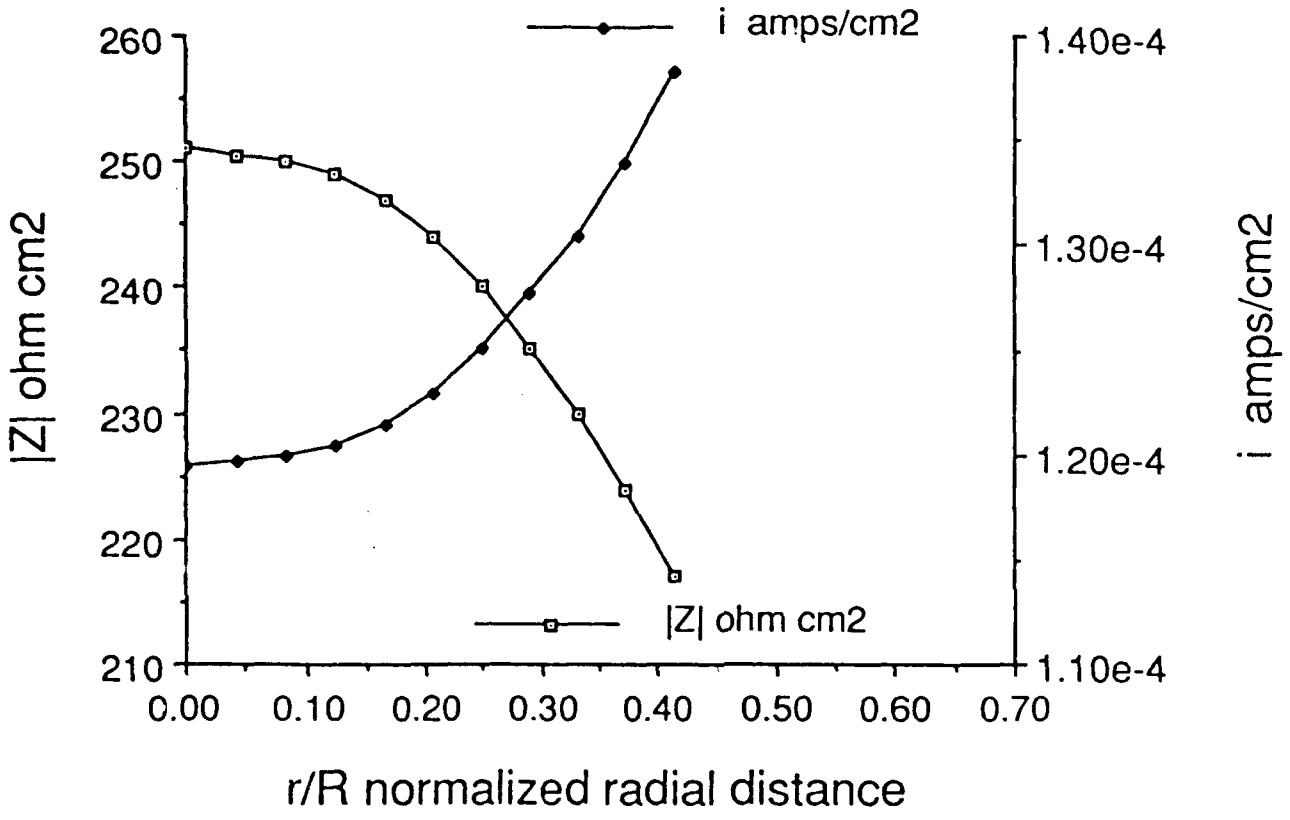

Figure 5 The variation of the magnitude of the impedance, and the corresponding ac current density, as a function of normalized radial distance at 6310 hertz for the aluminum electrode; **r** - distance from the center of the electrode **R** - radius of the electrode.

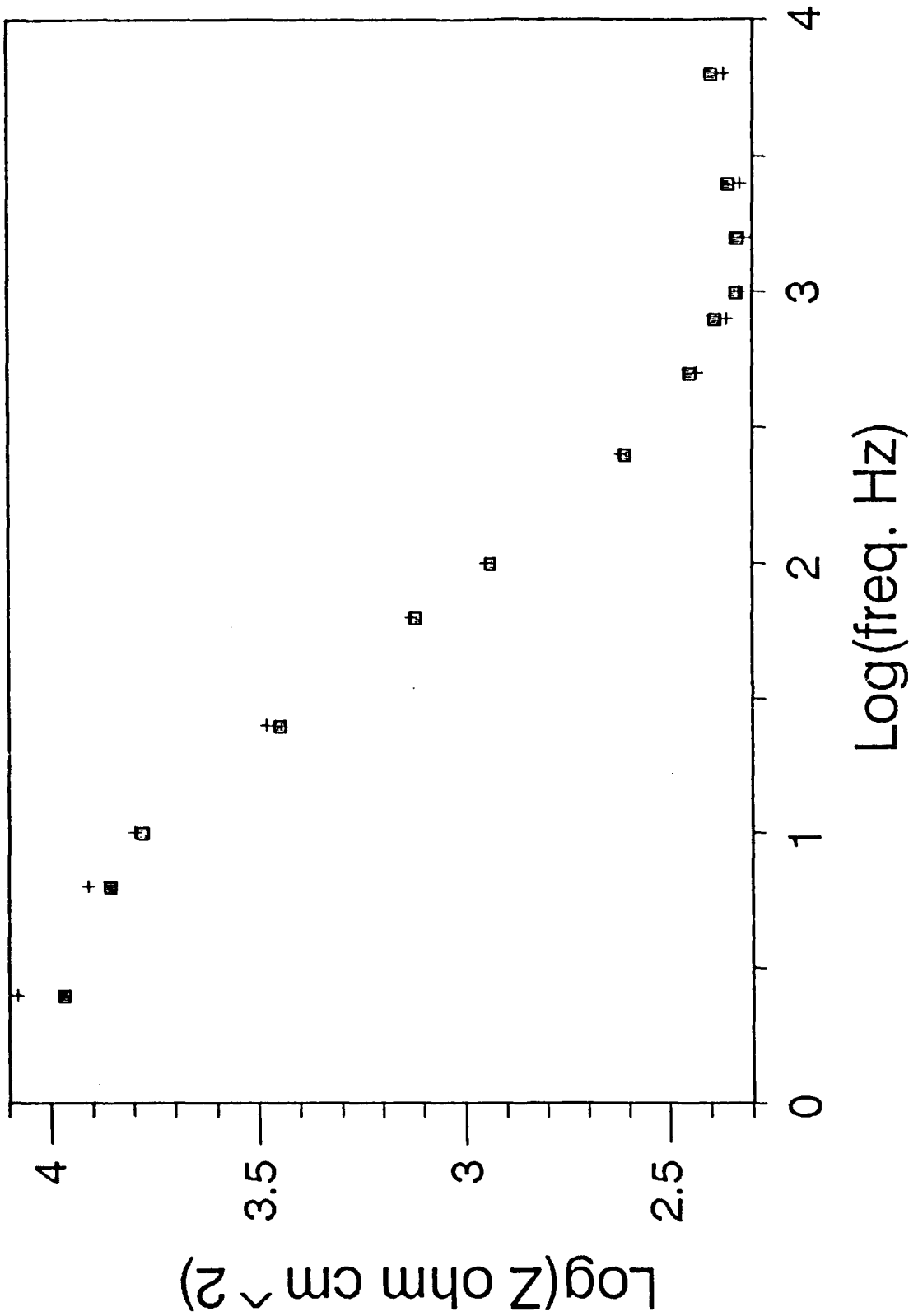

Figure 6 Bode Magnitude plots from LEIS measurements on the aluminum electrode. The (square) is from position X-1 in Figure 4 while the (plus) is from position X-2 .

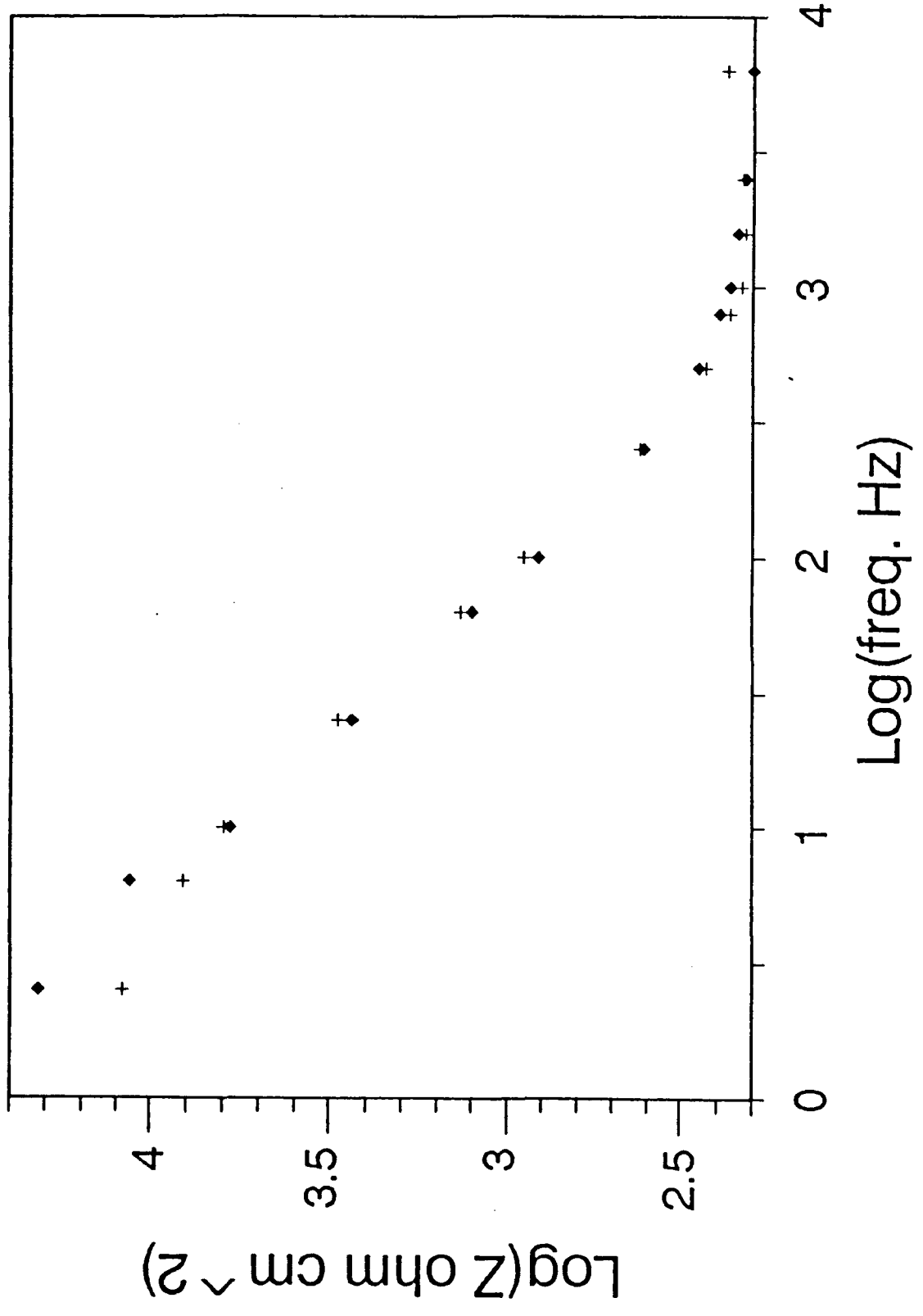

Figure 7 A comparison of the Bode Magnitude data for the aluminum electrode generated from LEIS measurements (plus) and traditional EIS (diamond).

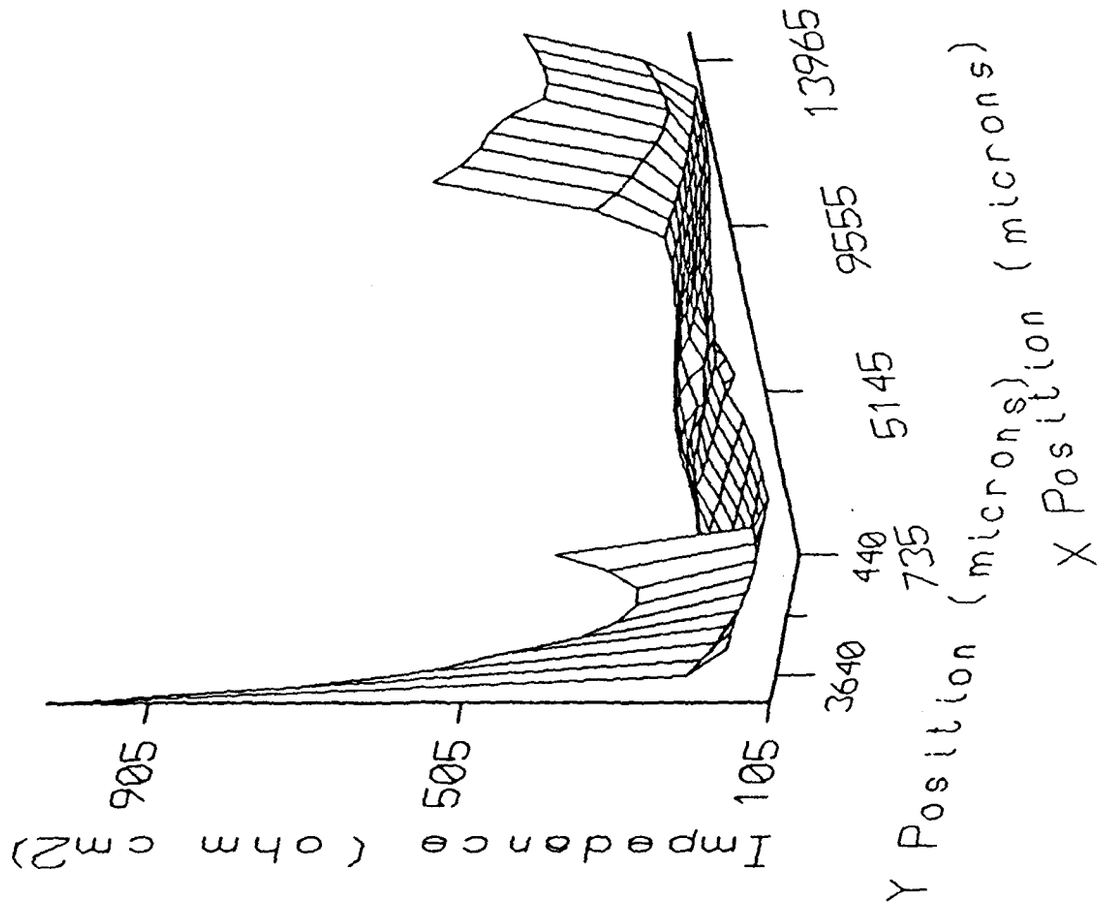

Figure 8 3-D maps of the magnitude of the impedance for the aluminum / molybdenum electrode generated with LEIS at **a)** 4677 hertz **b)** 4.7 hertz.

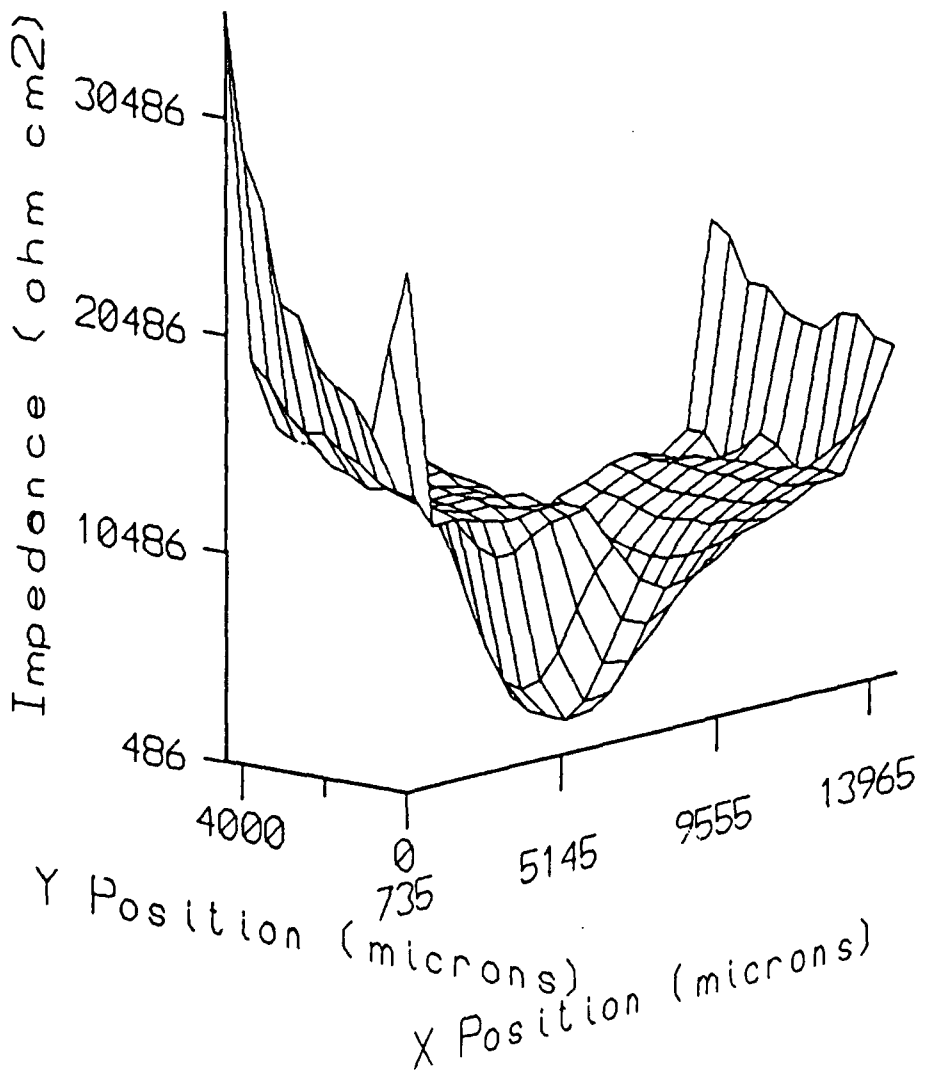
Impedance (ohm cm2)
30486
20486
10486
486
4000
0
735
5145
9555
13965
Y Position (microns)
X Position (microns)

Fig 5

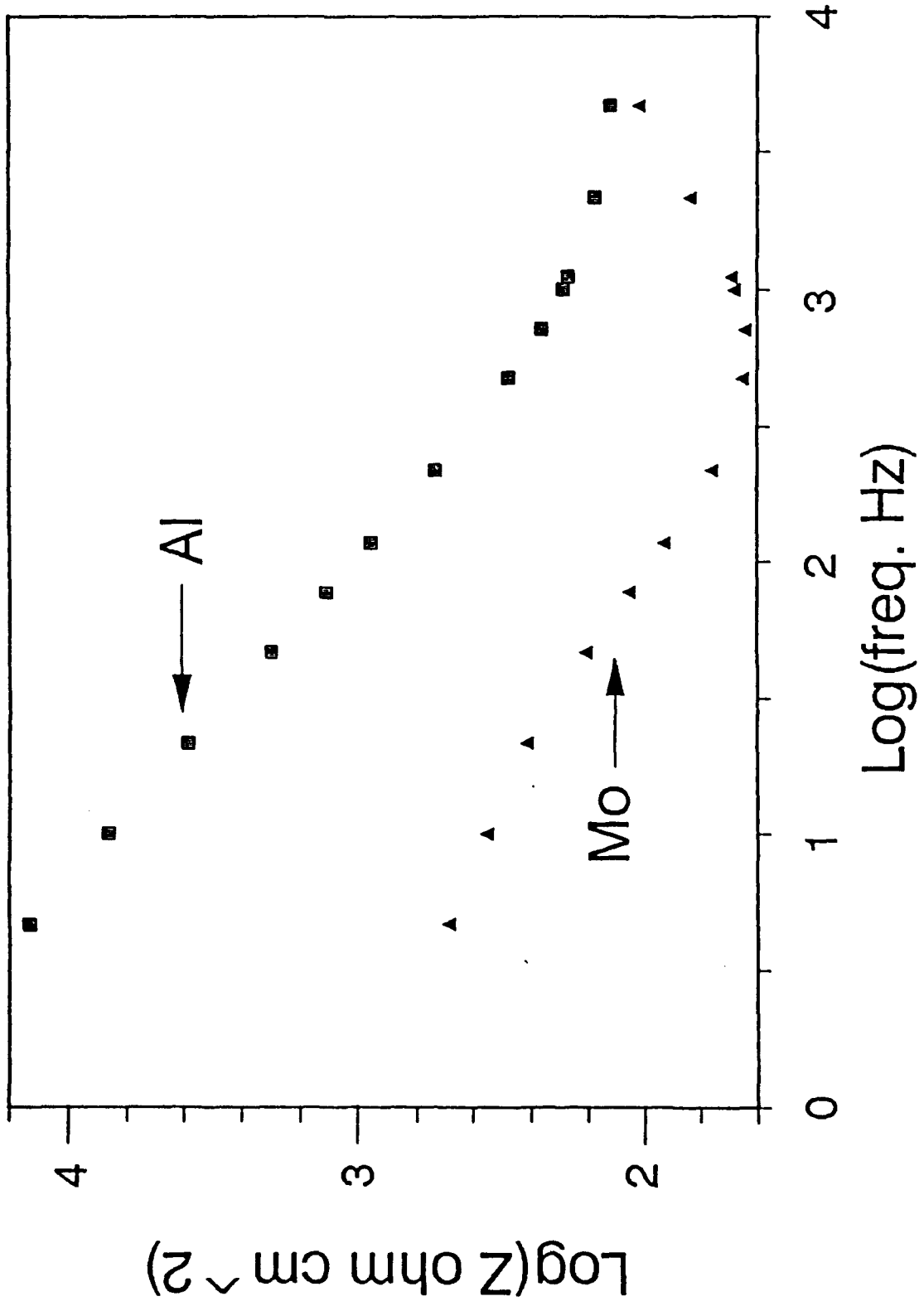

Figure 9 Bode Magnitude plots from LEIS data for the aluminum / molybdenum electrode. The (square) is from one position over the aluminum while the (triangle) is from one position over the molybdenum.

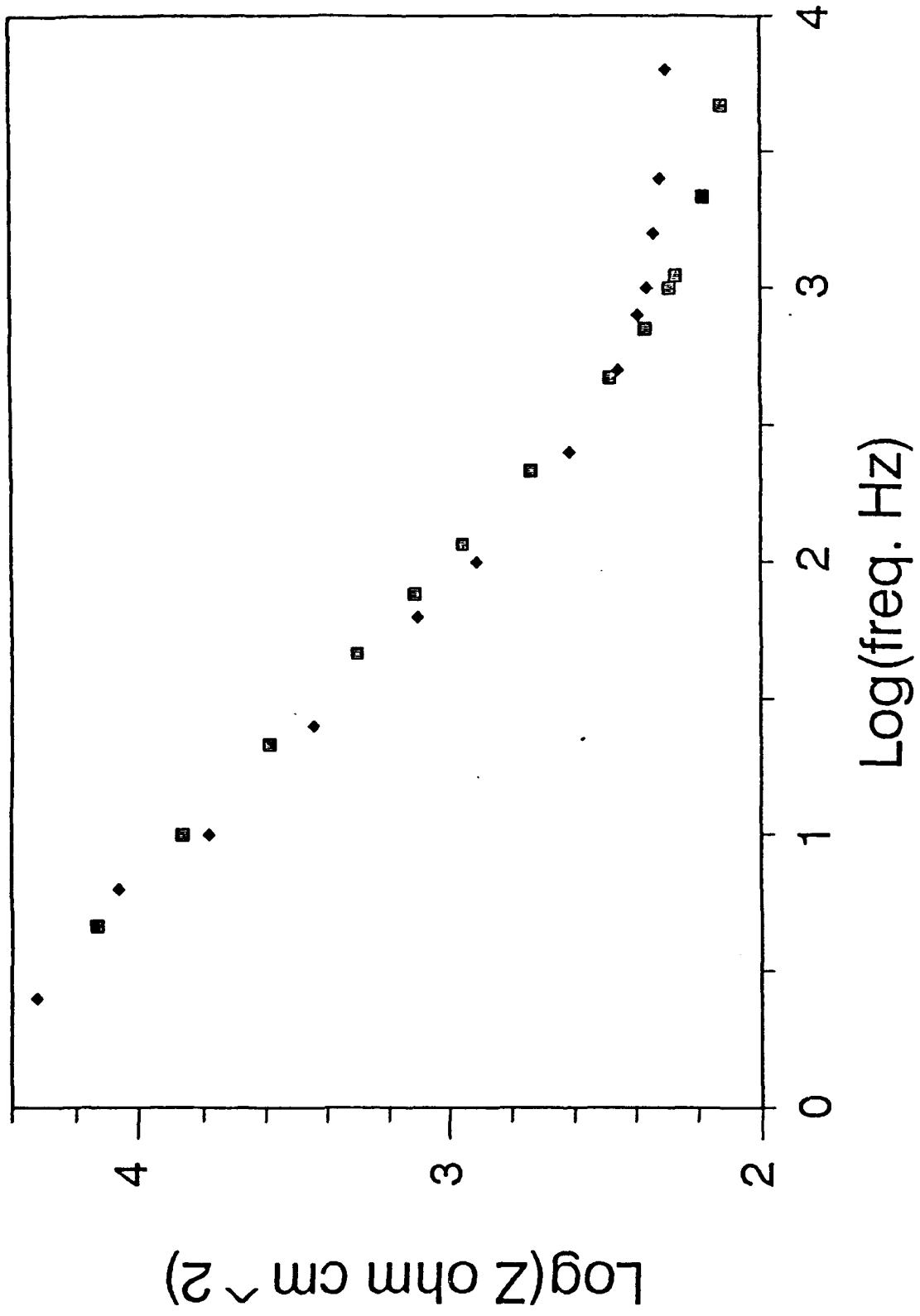

Figure 10 A comparison of the Bode Magnitude data from bulk aluminum (diamond) and one position over the aluminum portion of the Al/Mo electrode (square).